RF Studies for Ultrahigh Field MRI RF Coils and Arrays

by

Narayanan Krishnamurthy

BS, Mechanical Engineering, Regional Engineering College Warangal, 1996

MS, Computer Engineering, The George Washington University, 2003

Submitted to the Graduate Faculty of

Swanson School of Engineering in partial fulfillment

of the requirements for the degree of

Master of Science in Bioengineering

University of Pittsburgh

2019

UNIVERSITY OF PITTSBURGH

SWANSON SCHOOL OF ENGINEERING

This thesis was presented

by

Narayanan Krishnamurthy

It was defended on

January 25, 2019

and approved by

George D. Stetten, M.D., Ph.D.

Professor, Department of Bioengineering

Howard Aizenstein, M.D., Ph.D.

Professor Department of Psychiatry

Associate Professor, Department of Bioengineering,

Thesis Advisor: Tamer S. Ibrahim, Ph.D.

Associate Professor, Departments of Bioengineering, Psychiatry and Radiology

Copyright © by Narayanan Krishnamurthy

2019

RF Studies for Ultrahigh Field MRI RF Coils and Arrays

Narayanan Krishnamurthy, MS

University of Pittsburgh, 2019

Over the past few decades, different research groups have worked on different facets of Ultra-High Field (UHF) Magnetic Resonance Imaging (MRI); these developments culminated with the FDA approval of the first clinical 7 Tesla (T) MR scanner, Siemens MAGNETOM Terra in late-2017. MRI is still the preferred non-invasive multi-modal imaging technique for visualization of structural and functional correlates in-vivo and clinical diagnosis. Key issues with UHF MRI are in homogeneities in electric and magnetic fields as the size of imaged object becomes comparable with or larger than the radiofrequency (RF) wavelength. This inherent electromagnetic field inhomogeneity and elevated RF power deposition associated with UHF human imaging can have detrimental effects on the quality and safety in high field MRI.

To address these challenges, the research work presented in this study 1) evaluated different cylindrical loop receive (Rx) array geometry to establish their effect on the transmit (Tx) coil RF fields. 2) performed detailed analysis, phantom and in-vivo, comparing the performance of the Tic Tac Toe (TTT) coil with a 16-element Transverse Electromagnetic (TEM) coil using multiple anatomical head models and in-vivo.

The abovementioned areas of research included: Rx geometry model extraction from CAD models, and development of multiple anatomically detailed models and evaluation of MR coils simulations using full wave Maxwell's equations. Furthermore, an important part of the thesis work was bench marking of transmit coil performance for efficient and safe use in-vivo. The transmit arrays were tested for reproducibility, reliability and safe usage across multiple studies.

Finite Difference Time Domain simulations of the Tx and composite of five head models were used to optimize parameters, to obtain homogenous whole brain excitation with low RF absorption or specific absorption rate (SAR).

Table of Contents

List of Tables

List of Figures

Preface

I embarked in graduate work after I switched to a career in software and a bachelor's degree in mechanical engineering from Regional Engineering College Warangal. I am indebted to my family: mother, dad, brother and spouse, colleagues and mentors who have supported me in this endeavor. I have had the good fortune of working on multiple projects and making connections along the way. My research at the RF group at University of Pittsburgh with Professor Ibrahim at the helm began in fall of 2010. In 2012, I competed and won an NIH multimodal training fellowship award that involved cross modal image acquisition and analysis using MR and Near Infrared. Prior to this I had done rotations at BOSCH, the Computer Science department and a teaching fellowship at the Electrical and Computer Engineering departments (2004-2006). Prior to graduate school I worked as a software development engineer for DECT handsets at an IIT Chennai startup (1998-2001). I was an active student trainee at the Center for Neural Basis of Cognition, when at the University of Pittsburgh Bioengineering program. At the risk of not naming everyone I express my gratitude to all fellow students, and friends with whom I have had the pleasure of working, and still in touch.

1.0 Introduction

1.1 Review of Ultra High Field (UHF) Magnetic Resonance Imaging (MRI)

Magnetic resonance imaging (MRI) is a non-invasive, medical imaging modality used for clinical diagnosis, evaluation of treatment of disease in tissues of the human body. Decades of research in systems and sequences of MRI, has led to its use in visualizing different nuclei at unimaginable detail since Paul Lauterbur's 1974 article of imaging water capillary tube and the first in vivo image of thoracic cavity of a mouse (1).

The first clinical MR systems were installed in 1983 at low field strengths of 0.35, 0.5 Tesla (T), followed by the development of 1 T and 1.5 T magnets. Over the past 25 years, 1.5 T has been the main field strength in clinical settings (2). Over the last 10 years, 3 T MR scanners were introduced as a clinical modality. Increasing the magnet field strength has always been the driving force for improving the capabilities of MRI since the signal-to-noise-ratio (SNR) scales approximately linearly or even higher with the field strength (3). Increase in field strength, made it possible either to invest the increased SNR into reducing scan time or to obtain higher spatial resolution, for example. After the successful development of an 8 T MRI system at the Ohio State University in 1998, the first 7 T magnet was installed in the Center for Magnetic Resonance Research at the University of Minnesota in 2013 (4). After numerous installations since, there currently more than 65 7T research systems in operation worldwide. Although higher field strengths. i.e. 9.4T (5) and even higher (10.5 T) systems are currently available, 7T seems to have become the standard for ultrahigh field (UHF) MRI (6, 7), with U.S Food and Drug Administration

(FDA) approving its use on patients for clinical diagnostics in select applications (https://www.fda.gov/NewsEvents/Newsroom/PressAnnouncements/ucm580154.htm).

1.2 Objective and Outline of Thesis

Main issue at UHF MRI are in homogeneities in electric and magnetic fields as the size of imaged object becomes comparable with or larger than the radiofrequency (RF) wavelength. This inherent electromagnetic field inhomogeneity and elevated RF power deposition associated with UHF human imaging can have detrimental effects on the quality and safety in high field MRI. The major contributions in this thesis comprises of the JMRI and the PLOS one papers cited below. Additionally, included below are conference proceedings and other papers from both MRI and non-MR research projects, I have done or collaborated; as part of my work at the RF Research Facility at Pitt and neuroscience rotation during the bioengineering graduate program.

Papers:

1. **Krishnamurthy, N**., Zhao, T., and Ibrahim, T. S., "Effects of Receive-Only Inserts on SAR, B1+ Field and Tx Coil Performance ", Journal of Magnetic Resonance Imaging, Vol 39 pp 475-484, 2014.
2. **Krishnamurthy, N**., Santini, T., Wood, S., Kim, J., Zhao, T., Aizenstein, H.J., Ibrahim, T.S., "Computational and experimental evaluation of the Tic-Tac-Toe RF coil for 7 Tesla MRI", Plos One, Dec 2018, 10.1371/journal.pone.0209663.

Other Papers:

1. Zhao, Y., Zhao, T., **Krishnamurthy, N**., Zheng, H., Harris, C., Handler, W., Lin, S., Chronik, B., and Ibrahim, T. S. "Dual Optimization Method of RF and Quasi-Static Field Simulations for Reduction of Eddy Currents Generated on 7T RF Coil Shielding", Magnetic Resonance in Medicine. Vol 74, pp 1461-1469, 2015.
2. Raval, S., **Krishnamurthy, N**., Santini, T., Zhao, T., Britton, C., Gorantla, V. S. and Ibrahim, T. S. "Ultra-High Field Radiofrequency Coil Development for Evaluating Upper Extremity Imaging Applications", NMR in Biomedicine, Vol 29, 1768-1779, 2016.
3. Kim, J., **Krishnamurthy, N**., Santini, T., Zhao, Y., Zhao, T., Bae, K. T. and Ibrahim, T. S. "Experimental and numerical analysis of B1+ field and SAR with a new transmit array design for 7T breast MRI", Journal of Magnetic Resonance, Vol 269, pp 55-64, 2016.

4. Raval, S., **Krishnamurthy, N**., Santini, T., Zhao, T., C. Britton, Gorantla, V. S. and Ibrahim, T. S. "Ultra-High Field Upper Extremity Peripheral Nerve and Non-Contrast Enhanced Vascular Imaging ", Plos One, Vol 12 (6), pp 1-20, 2017.
5. Kim, J., Santini, T., Zhao, Y., **Krishnamurthy, N**., Zhao, T., Bae, K. T., and Ibrahim, T. S. "Development of a 7T RF Coil system for Breast Imaging", NMR in Biomedicine, Vol 30 pp 1-10, 2017.
6. Wood, S., **Krishnamurthy, N**., Santini, T., Raval, S., Farhat, N., Holmes, J. and Ibrahim, T.S., "Design and Fabrication of a Realistic Anthropomorphic Heterogeneous Head Phantom for MR Purposes", Plos One, Vol 12 (8), pp 1-16, 2017.
7. Santini, T., Kim, J., Wood, S., **Krishnamurthy, N**., Farhat, N., Maciel, C., Raval, S., Ibrahim, T.S., "A new RF Transmit Coil for Foot and Ankle Imaging at 7T MRI", Magnetic Resonance Imaging, Vol 45, pp 1-6, 2018.
8. Santini, T., Zhao, Y., Wood, S., **Krishnamurthy, N**., Kim, J., Farhat, N., Alkhateeb, S., Martins, T., Zhao, T., Aizenstein, H.J., Ibrahim, T.S., "In-vivo and numerical analysis of the eigenmodes produced by a multi-level Tic-Tac-Toe head transmit array for 7 Tesla MRI" Plos One, Plos One, Vol 13 (11), pp 1-16, 2018.

Presentations:

1. Godlove, J. M., **Krishnamurthy, N**., Faulkner, M., & Batista, A. P. (2009). A cross-modal reach redirection task in Rhesus monkeys reveals speeded processing for vibrotactile stimuli. Society of Neuroscience
2. **Krishnamurthy, N**., Bacher, D., McFerron, J. F. & Batista, A. P. (2009). "WiiMoCap: a low-cost motion capture system using the Nintendo Wiimote". Society of Neuroscience
3. **Krishnamurthy, N**., Zhao, T., Stough, D., Raval, S., Boada, F., Ibrahim, T. S. "B1+ and Coupling Variability of Transmit Head Coils and Arrays for Ultra-High Field MRI: Simulation Studies and Experiments", ISMRM 2012.
4. **Krishnamurthy, N**., Zhao, Y., Maccloud, R., Zhao T., Raval, S., Kim, J-H., Rosano, C., Aizenstein, H. & Ibrahim, T.S. (2014). Segmentation of Small Veins Using 3D isotropic SW images at 7T. ISMRM Milan 2014, 5788
5. Ibrahim, T.S., Santini, T., Raval, S., **Krishnamurthy, N**., Wood S., Kim J-H., Zhao Y., Wu X.S., Yacoub E.S., Aizenstein H., and Zhao T. (2017). Towards Homogeneous 7T Neuro Imaging: Findings and Comparisons between 7T TTT and NOVA RF Coil Systems. ISMRM, http://cds.ismrm.org/protected/17MPresentations/abstracts/4403.html(4403).

The outline of the thesis is as follows:

Chapter 2 provides background on MRI Sub systems, and RF simulations using FDTD modeling.

Chapter 3 provides analysis based on modeling different receive (Rx) geometry to establish their effect on the transmit coil RF fields (8).

Chapter 4 provides a detailed analysis, phantom and in-vivo, comparing the performance of the Tic Tac Toe (TTT) coil developed in-house with a 16-element Transverse Electromagnetic (TEM) coil using multiple anatomical head models and in-vivo (9).

2.0 Background – MRI Sub Systems

2.1 Static Fields – Superconducting Magnet

The image acquisition system comprises of a static field created by superconducting magnet. The precession frequency also called Larmor frequency (ω) is the rate the net magnetization vector of odd nuclei rotates in a static field. The precession rate is proportional to the static field strength, for instance H^1 precesses at 42.6, 127.7 & 297 Mhz in a static field of strength (1, 3 & 7 Tesla) respectively. The longitudinal equilibrium magnetization of a nuclei is proportional to proton density, electromagnetic quanta (hω) and Boltzmann statistic, for H^1 the magnetization parallel to static field is $\overrightarrow{M_0} = \frac{\rho\gamma^2 h^2 \overrightarrow{B_0}}{4kT}$, where ρ is proton density, γ is gyromagnetic ratio, h is plank's constant, k is Boltzmann's constant, T is temperature.

Spins and magnetization: Nuclei with odd number of protons and neutrons in nature possess a net spin angular momentum $\overline{S}$ the associated magnetic moment $\overline{\mu} = \gamma\overline{S}$, where γ is the gyromagnetic ratio of the nucleus in question. In medical imaging H^1 the hydrogen nucleus is abundant with gyromagnetic ratio γ 42.58 MHz/T.

Spin excitation and relaxation: The precessing spin of nuclei can be perturbed from equilibrium by applying an external, transverse RF field $\vec{B}_1$ with a rotation frequency that meets the resonance condition. If the pulse is applied for time $\tau = \frac{\pi}{2\omega_1}$, i.e. 90^o pulse the nuclei are

perturbed into the transvers (x-y) plane. The portion of $\vec{B}_1$ that rotates with Larmor frequency in the direction is ($\vec{B}_1^{+}$) and the portion that rotates in opposite direction is ($\vec{B}_1^{-}$).

$$\vec{B}_1^{+} = \frac{\vec{B}_{1,x} + i\vec{B}_{1,y}}{2} \quad \vec{B}_1^{-} = \frac{\left(\vec{B}_{1,x} - i\vec{B}_{1,y} \right)^*}{2} \tag{2.1}$$

After excitation the magnetization $\vec{M}$ starts to precess around $\vec{B}_o$, and the changing magnetic flux can be measured in a conducting loop, placed orthogonal to it. This voltage is the MR signal, called free induction decay (FID) (10). MR signal is affected by intrinsic and extrinsic factors; tissue relaxation (T1 & T2), proton density (ρ) are intrinsic to the tissue being imaged while coil/array transmit (B_1^{+}) and receive (B_1^{-}) sensitivity are external factors that also affect MR image quality. For example, the MR signal for a gradient echo sequence is given by:

$$\text{Signal} \propto F(T1, T2, \rho) * \sin(|B_1^{+}|) * |B_1^{-}| \tag{2.2}$$

The process of restoring thermal equilibrium of the perturbed magnetic moment is called spin relaxation, which is determined by two-time constants T1 & T2. T1 is the recovery of longitudinal Mz component referred to spin-lattice relaxation. The T2 referred to as spin-spin relaxation describes the loss of phase coherence of spins as they interact with each other. T2* refers to accelerated dephasing due to magnetic inhomogeneities and susceptibility, thus T2* < T2 < T1 holds for relaxation times (10) (11).

2.2 Gradient Fields

While the super conducting electromagnet creates the static field that causes the odd nuclei to precess (source of the MR Signal) and the gradient coils facilitate spatial selectivity, separate linear gradient coils in x, y, z directions alters the Larmor frequency of the nuclei of interest spatially, thus one obtains 2d slices which are in turn stacked in z to obtain 3d MR images.

2.3 Transmit (TX) and Receive (RX) Coils

The current work focuses on the Transmit & Receive MR coils, its performance evaluation using RF full wave simulations and experiments with phantom and in-vivo. The RF coil generates a spatially dependent $\vec{B}_1(\vec{r})$ field by an electric current (I); for an infinitely long conductor Bio-Savart law gives the direction and strength of magnetic field with displacement vector $\vec{r}$: $\vec{B}_1(\vec{r}) = \frac{\mu_0 I}{4\pi}\int \frac{d\bar{l}x\vec{r}}{|\vec{r}|^3}$. For optimal power transfer between the source (amplifier) and RF coil, impedance matching is needed, the conjugated impedance (Z^*) of the amplifier has to match the transformed impedance (Z) of the RF coil (typically 50Ω). Z is made of real and imaginary parts (resistance & reactance). Coil resistance consists of 1) ohmic resistance is dependent and conductor conductivity (σ) and dimensions (length and diameter) $R_\Omega \propto \frac{\sigma L}{\varnothing_d}$, 2) radiation losses $R_r \propto \omega^4 Area^2$, and 3) tissue losses R_t that represents power absorbed in conductive tissue due to induced current and electric field displacement currents.

Evaluating Transmit and Receive coils at UHF for MRI at 7T has been the focus of several research groups (6, 12-18). The transmit and receive coils though interconnected by the reciprocity law of electromagnetics, have different requirements. The transmit array is required to produce a homogenous spin excitation; in our experience a highly coupled transmit array one can obtain a homogenous spin excitation, that is more stable to changes to RF loading or subject insensitive than other transmit coil designs. In contrast, decoupled independent observers are best suited to discern and uncover a signal corrupted by noise. Thus, one goes to great lengths to ensure both the coils are decoupled of each other when used in conjunction.

2.4 RF Simulations

2.4.1 Maxwell's Equations

Full wave Maxwell's equations that couple electric and magnetic fields is given by the four equations that govern physics of electromagnetic waves in media are:

$$-\frac{d\bar{B}}{dt} = \nabla x\bar{E} + \sigma_m \bar{H} \quad \text{(Faraday's Law)} \tag{2.3}$$

$$\frac{d\bar{D}}{dt} = \nabla x\bar{H} - \sigma_e \bar{E} \quad \text{(Ampere's Law)} \tag{2.4}$$

$$\nabla \bullet \bar{D} = \rho, \quad \nabla \bullet \bar{B} = 0 \quad \text{(Gauss's Law)} \tag{2.5}$$

$$\bar{D} = \epsilon \bar{E}, \quad \bar{B} = \mu \bar{H}, \quad \bar{J} = \sigma \bar{E} \text{ (Constitutive Relations)}$$

(2.6)

Where the divergence $\nabla \bullet \bar{D} = \oiint D \bullet d\bar{A}$ and curl operator $\nabla x \bar{E} = \oint \bar{E} \bullet d\bar{l}$ are given as:

$$\nabla f = \frac{df}{dx}\bar{i} + \frac{df}{dy}\bar{j}\frac{df}{dz}\bar{k} \quad \nabla x\bar{f} = \begin{vmatrix} \bar{i} & \bar{j} & \bar{k} \\ \frac{d}{dx} & \frac{d}{dy} & \frac{d}{dz} \\ \bar{p} & \bar{q} & \bar{r} \end{vmatrix}$$

(2.7)

Stokes theorem: $\oint_C F \bullet dr = \iint_S curlF \bullet dS$

(2.8)

2.4.2 Finite Difference Time Domain (FDTD) – Iterative Computation of Fields

Electric and magnetic (E and H) fields are interdependent and functions of space and time and Yee's FDTD algorithm was used to calculate both in a leap frog scheme iteratively (Figure 1). The new E value in the current location is dependent on the E in the same location from previous time step and the surrounding H values. Similarly, H depends on previous H and surrounding E values. Thus, by staggering E(x, y, z) and H(x, y, z) by half a cell size Yee proposed to compute E & H fields iteratively in space with time (19).

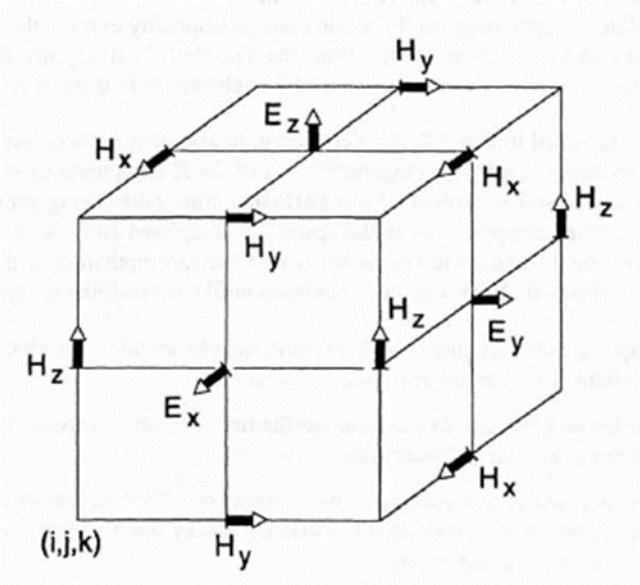

Figure 1: Yee – Grid: Surrounding H used to compute E and vice-versa

The computational domain consists of discretized voxels of tissue and or coil elements and sources and termination layer or perfectly matched layer (PML) that absorbs incident waves on its surface and prevents reflections from the end of domain (Figure 2). The dielectric properties of different tissues in frequency range 10Hz–100GHz is obtained from (20-23). http://niremf.ifac.cnr.it/tissprop/. Figure 3 shows an example of EM wave propagation from four sources in a human body.

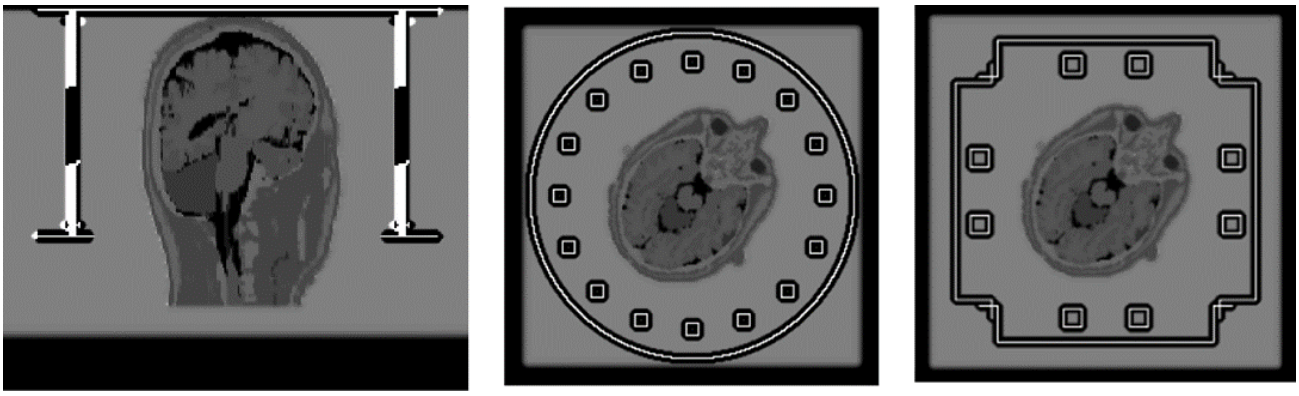

Figure 2: 3d Voxel Models of TEM and TTT coils: Computation domain of 1.6mm voxel size was created with constituent property of air or coil (comprising of copper, dielectric) or anatomically detailed head model. Computation domain ends with layers of perfectly matched layers (PML) that prevents reflection of RF from end of domain. Coil is tuned to 297Mhz by adjusting copper length inside the dielectric

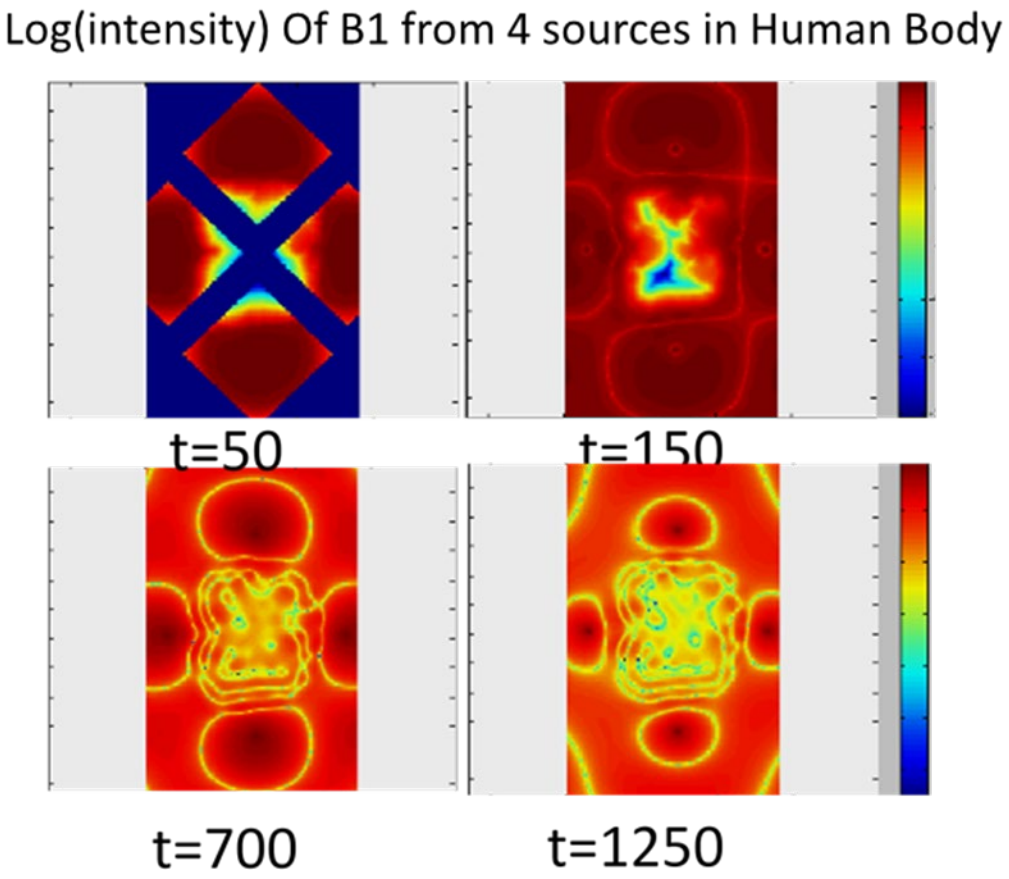

Figure 3: FDTD Simulations : Progression of a transient pulse through the domain, from four sources, in an anatomically detailed body model

2.4.3 RF Safety Assurance

RF power absorbed per kilogram of tissue, termed specific absorption rate (SAR) is used to set safety limits for in-vivo imaging, given tissue temperature in the dynamic system (with conduction and perfusion and other thermodynamic effects) is difficult to ascertain. The electric field $\vec{E}$ causes an induced current density $\vec{J} = \sigma \vec{E}$; the power thus deposited in the tissue,

$$P = \int \sigma E^2 dV = \frac{1}{4} \sigma B_1^2 \omega^2 \int r^2 dV$$

(2.9)

and specific absorption rate (SAR):

$$SAR = \frac{\sigma}{\rho} E^2 \propto B_1^2 \omega^2$$

(2.10)

From equation 2.10, doubling the magnetic field or pulse flip angle will quadrupole the SAR. Thus, high field strengths and inversion or 180^o pulses used in clinical imaging e.g. turbo spin echo are limited by the absorption limits set by National and international standards, IEC 6061-2-33 stipulates: The average SAR may not exceed 4W/Kg for body and 3.2W/kg for head imaging. Local maxima in SAR (averaged over 10g of tissue) are allowed up to 10W/kg for head and trunk and up to 20W/kg for the extremities (24).

3.0 Effect of RX Copper on TX Fields

3.1 Compare Effects of Cylindrical RX Only Arrays on TX Fields

3.1.1 Background

Parallel transmit and receive systems have been built for high and ultrahigh field MRI. Dedicated transmit and receive systems have been designed to handle the challenges that arise at high frequencies when the sample becomes electrically large compared to the operating wavelength. While RF inhomogeneity is handled by designing better transmit-only arrays and shaping transmit wave forms (shimming) to obtain homogenous spin excitation. Close fitting decoupled receive-only arrays have been built to increase the signal to noise ratio (SNR) and acceleration in acquiring MR images. Although highly sensitive, multichannel receive-only array for high field MRI have been built.

Static fields up to 8T have been shown to have no serious health effects. Several studies by (25, 26) on gradient coils and of movement in high fields have been done as part of safety assurance of MR systems. Food and Drug Administration (FDA) and International Electro-technical Commission (IEC) have guidelines in evaluating multi-channel Tx/Rx systems. Receive array geometry have grown in number from 8 to 32, 64, and 96 channels (27, 28), with corresponding increase in copper and circuitry (passive detuning elements) associated with it. As the copper coverage of Rx loop array increases there is a concern, the detuned Rx circuitry would scatter the transmit coils RF fields.

Prior work on safety assurance of multimodal electroencephalography and functional imaging (EEG-fMRI) has shown currents induced on closely conforming leads/electrodes caused an increase in radiofrequency (RF) absorption (29, 30). An earlier study done on a phantom at 3Tesla showed a SAR increase on a rectangular phantom in a Tx birdcage coil with the presence of 2 Rx-loops (31).

There are few studies that look at the influence of close conforming receive-only arrays on the transmit coil performance; and assure the combination of Tx and Rx arrays are safe to use. Here, using numerical simulations and experimental verifications we look at the effect of different receive-only insert designs such as 8 and staggered 16 cylindrical arrays and its effect on the transmit RF field (spin excitation field defined as B_1^+ field) and specific absorption rate: SAR of a 7Tesla transverse electromagnetic (TEM) coil.

3.1.2 Methods

To test the effect of Rx geometry and copper trace widths: We developed finite difference time domain (FDTD) models of different cylindrical receive-only array geometries (8 and staggered 16) with varying copper trace widths (3.2 and 6.4mm wide), a TEM Tx coil model with 8 elements was used in the study, and two head models were used in numerical simulations. Tx coil coupling was experimentally measured and validated with FDTD modeling.

3.1.2.1 FDTD Models

The 3-dimensional computational domains with isotropic resolution of ~1.6mm was constructed by setting the constitutive properties to that of the RF coil (comprising of Rexolite or, Teflon, or Copper) or to the different tissues of the anatomically detailed head models. Spatial

resolution 1.6 mm λ (< l/20) and temporal resolution of ($\Delta t < 3e^{-12}$) was used for simulation as per Courants stability criterion (32).

The coil model has a true transmission line model for the excitation elements with accurate modeling capability of the coil's input impedance and coupling (33).The numerical models of the coils were tuned to Larmor frequency of 7T (300 MHz) using an anatomically detailed head model by adjusting the gap between the inner coaxial elements of the 8 element TEM Coil whose schematic is shown in Figure 4. FDTD models of the TEM transmit coil and different receive-only inserts used in full wave simulations at 7 T are shown in Figure 5. The computational domain was terminated using 32 layers of perfectly matched layer (PML) with electric and magnetic losses as per Berenger (34) to minimize reflections from the end of the domain. The computational domain was constructed by setting the constitutive properties of the Yee cell (15) to conductivity (s) and dielectric constant (εr) corresponding to one of 22 or 19 tissue types, air, copper, or Teflon. Two head models, model 1 of 19 tissues and 3.6 kg, and model 2 of 22 tissues and 4.7 kg, were used in the simulations. Model 2 was 30% larger than model 1 in terms of volume. The RF shield, inner and outer coaxial copper, and receive array loops were modeled as a perfect electric conductor (PEC), with their tangential component of electric field set to zero.

Electric (E) and magnetic (H) field computations based on Maxwell's equations in differential form were obtained with second-order accurate central difference estimates on the 3D Yee grid, at spatial intervals of d/2 and temporal intervals of dt/2 in a leapfrog manner. The value of a component of E (or H) at any position can be determined from its previous value and the previous values of H (or E) components at adjacent grid positions (35).

3.1.2.2 TEM 8 Element FDTD Model and Measurements

A transverse electromagnetic (TEM) resonator was used for the transmit coil. The transverse electromagnetic resonator coil is made of 8 coaxial resonators located 45 degrees apart between two circular rings (9' internal and 13' external diameter). The resonator is encased in an outer RF shield to minimize transmit voltage required to produce resonance and saturation of spins (flip angle > 90^{o}). This distributed coaxial resonator is robust, and efficient when compared to lumped element birdcage resonators at high frequencies (36). Four of the ports of the coil were connected in quadrature to produce circular polarization. Voltage per port was scaled by the reflection seen by the port (S_{xx}) to equalize transmission across ports ($\sqrt{1 - S_{xx}^2}$).

3.1.2.3 Cylindrical Overlapped 8 and 16 Loop Arrays with 3.2/6.4mm Wide Copper

Cylindrical overlapped 8-loop and staggered 16-loop array geometry conformed to a cylinder of 9inch diameter and 6inch height. We modeled cylindrical receiver geometries as they are the most prevalent designs used in MRI. Active and passive detuning of loops in array (2 per loop for 16 and 4 per loop for 8-loop array) were modeled as open circuit. Rx-only array detuning ensures the receiver is decoupled from the transmit coil. Detuning minimizes the effect parallel closely adjoining copper from Rx-array has on the transmit field and primarily is used to protect the preamplifiers when hundreds of volts are applied during excitation at the transmit coil. The loop copper of the Rx-only array is modeled as flat perfect electrical conductor (PEC). To test if copper trace width had any effect on the TEM coil transmit field, copper width of the 8 and 16-loop array were varied from 3.2 to 6.4mm.

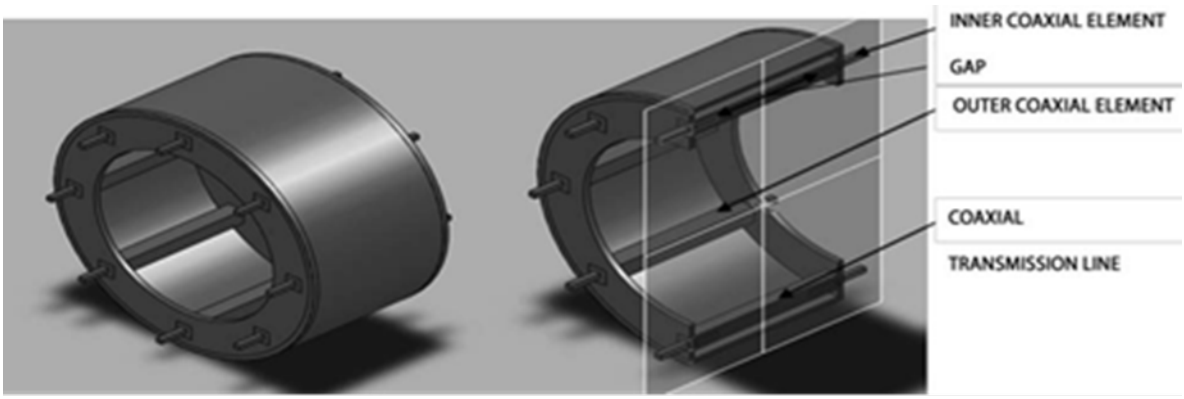

Figure 4: Schematic of an 8-element TEM coil resonator is shown. The resonator ports were tuned and matched at 297 MHz by adjusting the gap between the inner coaxial elements. Four active ports of the coil were connected in quadrature in order to produce circular polarization.

Cylindrical Loop Arrays Geometries: 8 and staggered 16

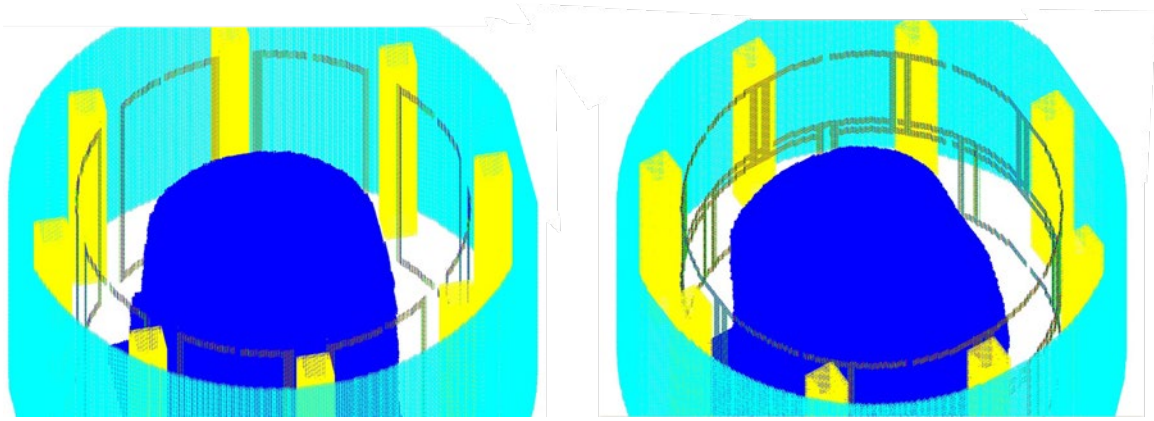

Figure 5: Geometry of different receive-only inserts: Cylindrical overlap 8-loop, staggered overlap 16-loop arrays. Copper was modeled as flat perfect electrical conductor (PEC). Active and passive detuning elements per loop were modeled as open circuit. Two anatomically detailed head models of 1.6 mm resolution; one 30% larger (in terms of volume) than the other was used in the simulations. Model 1 is composed of 19 tissues and has 3.6 kg mass; Model 2 is composed of 22 tissues and has 4.7 kg mass. The 8 and staggered 16 loop array geometries were modeled with copper trace width of 3.2 and 6.4mm to test the effect of copper width on the transmit fields

3.1.2.4 RF Absorption

The specific power absorption rate ($P = 0.5\sigma E^2/\rho$ in W/Kg) is a function of sample size (m), geometry of coil, MR frequency, RF pulse duration (τ), repetition time (TR), tissue conductivity (σ), dielectric constant (ε) and density (ρ) (37). The whole-body absorption and radiation from a transmit coil during a MRI scan can be obtained accurately by measuring 1) the output power from RF amplifier, 2) measuring cable loss to the transmit coil and 3) measuring

reflection at the transmit coil ports with the subject. The incident power on the subject is (1-reflection^2). While whole body absorption can be accurately obtained from experiments, local peak in absorption can only be determined using numerical simulations. RF hot-spots are created due to uneven distribution of RF power in association with restrictive conductive patterns to flow (38). Hot-spot ratios (peak SAR/mean SAR) > 20 have been reported even at 3Tesla (39). Manufacturers and system designers must meet the regulatory stipulate of SAR averaged over 10gm average of tissue, even if actual temperature rise due hot-spots is dependent on heat dissipation due to perfusion etc.

3.1.3 Analysis of Effects of Different Cylindrical RX Array on TEM RF Fields

3.1.3.1 Changes in Scatter Parameters in 2 Head Models

The TEM coil simulations have been validated to produce excellent match with experimentally obtained transmit and receive field maps (33, 40). Figure 6 shows a successful match in scatter parameters obtained from a network analyzer with those obtained from full wave FDTD simulations. The TEM coil model was tuned to 300 MHz by adjusting inner copper lengths in the model. Shift in resonant frequency with different receive-only inserts was < 3MHz in numerical simulations. The coupling between adjacent (S_{12}) and opposite (S_{13}) ports for the two head models when different receive-only inserts were used are summarized in Table 1. Percent change in coupling was less than 6% for the different cases. Thus, the existing receive-only array designs minimally alter the coupling between ports of the TEM Tx coil.

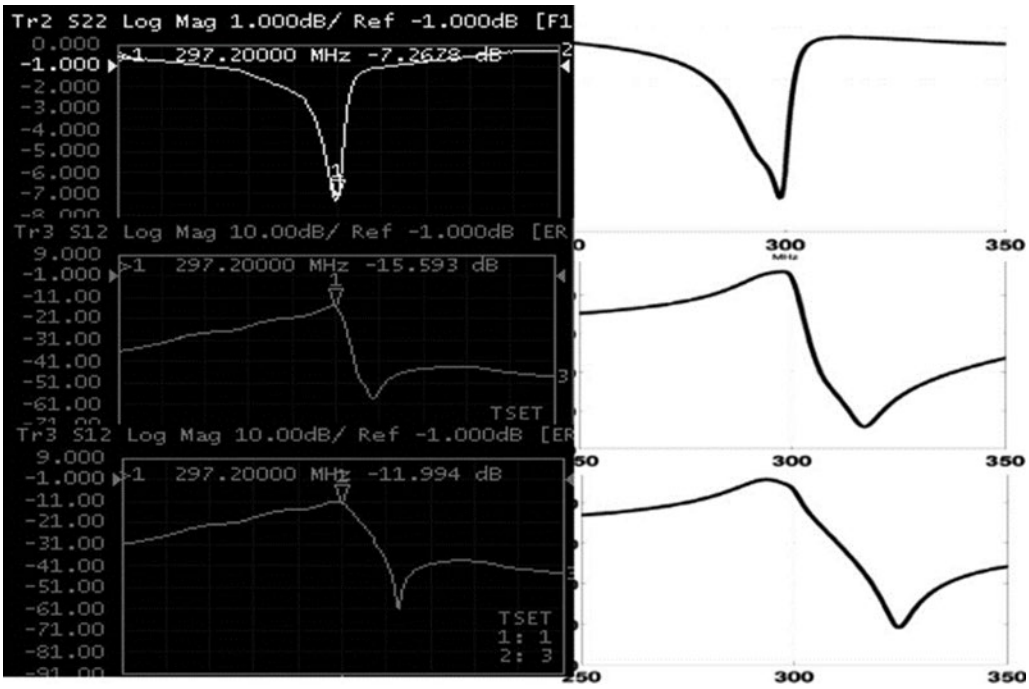

Figure 6: Validation of FDTD Scatter Parameters with Bench Measurements: Scatter parameters obtained by a network analyzer and from FDTD simulations. The 8-element TEM resonator and its computational model were tuned and matched to a human head model at 300 MHz by adjusting the gap between the inner coaxial elements. The measurements and numerical simulations of the reflection and coupling demonstrate very good agreement.

Table 1: Effects of Rx-Only Inserts on TEM Coil Scatter Parameters (Simulation Results): TEM coil resonant frequency shows minimal shifts (< 3 MHz) when Rx inserts were used in simulations. Transmission values at 300 MHz from numerical simulations of coupling between adjacent ports (S12) and opposite ports (S13) for the two heads with different receive inserts are summarized. The coupling between ports of TEM coil minimally changes when different receive inserts were used (< 6%). The reflection of two ports of TEM coil and the changes with different Rx-inserts are also shown. The maximum change in reflection was < 13%. The TEM coil model was not retuned for different Rx inserts but voltage of each port was scaled for equal transmission.

	Scatter parameters head model 1 (dB)					Scatter parameters head model 2 (dB)				
	h1	8-loop		16-loop		h2	8-loop		16-loop	
		3.2mm	6.4mm	3.2mm	6.4mm		3.2mm	6.4mm	3.2mm	6.4mm
s22	6.99	5.96	6.13	6.79	6.69	6.57	5.96	6.11	6.45	6.45
s44	7.25	6.18	6.36	6.74	6.59	6.45	5.83	5.96	6.41	6.41
s12	15.88	16.36	16.22	15.71	15.66	16.74	17.24	17.09	16.57	16.57
s13	11.36	11.89	11.77	11.37	11.4	12.65	12.63	12.51	12.18	12.18
		% change in magnitude					% change in magnitude			
s22		12.59	10.42	2.34	3.54		7.23	5.43	<2	<2
s44		13.11	10.84	6.09	7.95		7.39	5.72	<1	<1
s12		5.4	3.8	<2	2.6		5.6	3.9	2	2
s13		5.9	4.6	<-1	<-1		<2	<2	5.6	5.6

3.1.4.1 Changes in B_1^+ Distribution

Figure 7 (a, b) shows sagittal and coronal slices of B_1^+ from FDTD simulations on an anatomically detailed head model without and with Rx-only inserts. Figure 7 (c, d) shows in vivo B_1^+maps obtained at 7 T in a TEM coil without and with a 14Ch Rx insert conforming to the head. The B_1^+ distribution without and with the Rx inserts remained similar both qualitatively and quantitatively, thus the Rx inserts do not degrade the spin-excitation performance of the TEM coil. The smaller (head2) head has a higher mean B_1^+ than the larger (head3) head (0.8 versus 0.6 micro Tesla). Table 2 summarizes the percent change in B_1^+ field when different receive-only inserts were used. The changes in peak, ratio of max/mean and coefficient of variation of B_1^+ in the brain were minimal (< 4%) when different Rx-only array inserts were used. Thus, while total absorption and B_1^+increased (as will be discussed in the next section) and radiation decreased with different receive-only inserts; mean B_1^+ field per 1 Watt of absorption did not change.

Table 2: Effects of Rx-Only Inserts on B_1^+ Distribution of TEM Coil: B_1^+ in brain were calculated for 1 watt absorbed power and 1 watt real forward power. The B_1^+ distribution for 1 watt absorption in the brain did not change appreciably when different receive inserts were used (< 4%). Subtle changes in B_1^+ distribution (< 14%) were observed with different receive inserts for the same real forward power

		B1+ per 1 watt absorbed power mean(μT), CV				B_1^+ for 1 watt forward power mean (μT)		Percent change in B_1^+ per 1 watt absorbed power mean(μT), CV			Percent change in B_1^+ per 1 watt forward power mean(μT)		
		H1		H2		H1	H2	H1		H2	H1		H2
Cylindrical Arrays	Head Only	0.76	0.29	0.6	0.27	0.68	0.53						
	Head+8-loop array copper width 3.2 mm	0.76	0.3	0.59	0.27	0.74	0.58	0	3	-2	0	9	9
	Head+8-loop array copper width 6.4 mm	0.76	0.3	0.59	0.27	0.73	0.57	0	3	-2	0	7	8
	Head+16-loop array copper width 3.2 mm	0.79	0.29	0.61	0.27	0.75	0.58	4	0	2	0	10	0
	Head+16-loop array copper width 6.4 mm	0.79	0.29	0.61	0.27	0.77	0.58	4	0	2	0	13	9

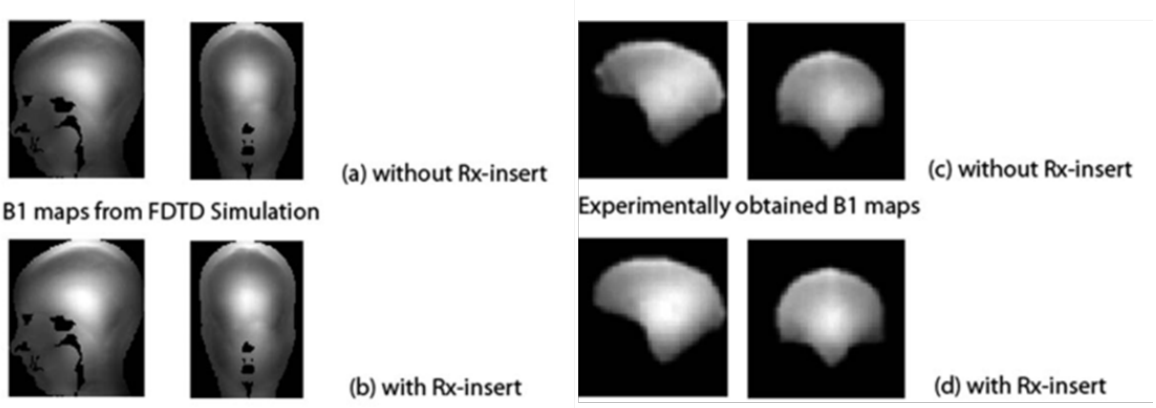

Figure 7 : Effect of Rx inserts on B_1^+ distribution, simulation, and experimental results. Sub figures (a) without Rx insert and (b) with Rx insert show sagittal and coronal slices of B_1^+ from FDTD simulation in an 8-element TEM coil with four active ports connected in quadrature and a 32Ch helmet Rx insert. Subfigures (c) without Rx insert and (d) with Rx insert show sagittal and coronal slices of B_1^+ obtained at 7 T using a 16element TEM coil with four active ports connected in quadrature and a 14Ch helmet Rx insert. The B_1^+ distribution without and with the Rx inserts remain similar for both simulation and experiments. Note: the coil (both Tx and Rx) used for experimental verification of effect of Rx inserts on B_1^+ field are different. from the FDTD models used in the study.

3.1.4.2 Changes in Global Absorption

Total absorbed power in the head is given by $\sum 0.5\sigma |E^2|$ over the entire human head model. SAR (Watts/Kg) per 10gm of tissue in the two head models for mean 2μTesla B_1^+ in brain and for 1-watt forward power were computed.

Table 3 and Table 4 summarizes RF absorption in the heads with different receive-only array inserts; there was a 9-18% increase in absorption in the 2 heads when different Rx-only array inserts were used. Conservation of energy indicates Input Real power = Absorbed power +

Radiated power. Thus, for equal input power an increase in the RF absorption in the head models would imply a decrease in radiation from the TEM coil. Changes in Global Absorption with Copper Trace Width: shows the change in RF absorption in the two heads and 9 tissues that constitute 80% of total absorption, when different Rx-only inserts were used. The overall effect of copper trace width on RF absorption was small (<5%); total absorption increased for staggered 16-loop array, while it decreased for the 8-loop array.

3.1.4.3 Changes in SAR Distribution

Figure 8 shows Sagittal slices in the two head models plotted at the peak local SAR location. The percent change in SAR from the base case without the 8 & 16loop arrays, and changes in SAR with the presence of detuned loop arrays are clearly highlighted in Table 3 and Table 4.

To analyze the regions with an increase in SAR, the percent change plot was overlaid with conductivity of different tissues at 300 MHz. The SAR increased at regions with tissues with widely different conductivity. Regions adjoining sinuses and at boundary of tissues like CSF, Bone, Eyes and GM show notable increase in SAR.

The boundary conditions at the interface of two media predicts a possible pileup of charges at the interface corresponding to the difference in normal electric field component; the potential difference due to the boundary conditions form the driving potential for RF currents to flow, with different tissues offering varying resistance to flow of current. Thus, the electric fields and induced RF currents in the tissue determine the hot-spot locations in the head models.

Table 3: Effects of Rx-Only Inserts on Global SAR in Head Models: Total absorption in head models were calculated for allowable peak local SAR of 10 W/kg per 10 g and 1 watt real forward power. Changes in absorption for the same real forward power indicate a change in radiation of the TEM coil when the different RX-only arrays were used. Total absorption per watt forward power increased (14 to 21%) for the 8 and 16 loop cylindrical arrays

		Total absorbed power (W) for peak local SAR= 10 W/kg per 10 g		Total absorbed power (W) for 1 watt forward power		Percent change in total absorbed power (W) for peak local SAR= 10 W/kg per 10 g		Percent change in total absorbed power for 1 watt forward power	
		H1	H2	H1	H2	H1	H2	H1	H2
	Head only	10.14	12.49	0.78	0.8				
Cylindrical Arrays	Head+8-loop array copper width 3.2 mm	11.35	13.76	0.94	0.95	11.83	10.12	21	19
	Head+8-loop array copper width 6.4 mm	11.2	13.58	0.92	0.93	10.41	8.74	18	16
	Head+16-loop array copper width 3.2 mm	11.68	14.37	0.92	0.91	15.15	15.07	18	14
	Head+16-loop array copper width 6.4 mm	12.01	14.37	0.94	0.91	18.42	15.07	21	14

Figure 8 and Figure 9 shows the changes in peak SAR intensity (averaged over 10gm of tissue for a mean B_1^+ field in brain of 2μ Tesla) in the two head models when different receive-only array were used. The peak local SAR or hot-spot location and intensity in some tissues changed when Rx-only inserts were used. The peak SAR shows an overall increase for the 8-loop array. The staggered 16-loop array had minimal change in its peak SAR distribution.

Table 4: Effects of Rx-Only Inserts on Local SAR in Head Models: SARs were obtained for mean B_1^+ in brain of 2 μT and 1 watt real forward power. Peak local SAR intensity in the head models changed when the different RX-only array were used. Peak local SAR changed 1 to 8% for the same B_1^+ in brain and 19 to 31% for the same real forward power

		Peak local SAR for mean B1+ 2 μT in brain (WM+GM+CSF+ midbrain+ cerebellum)		Peak local SAR for 1 watt forward power w/kg per 10 g		Percent change in peak SAR for mean B1+ 2 μT in brain (WM+GM+CSF + midbrain+ cerebellum)		Percent change in peak SAR for 1 watt forward power	
		H1	H2	H1	H2	H1	H2	H1	H2
	Head only	6.72	8.99	0.77	0.64				
Cylindrical Arrays	Head+8-loop array copper width 3.2 mm	7.2	9.68	0.98	0.81	7.14	7.68	27	27
	Head+8-loop array copper width 6.4 mm	7.17	9.65	0.95	0.79	6.7	7.34	23	23
	Head+16-loop array copper width 3.2 mm	6.83	8.95	0.97	0.76	<2	<-1.0	26	19
	Head+16-loop array copper width 6.4 mm	6.85	8.95	1.01	0.76	<2	<-1.0	31	19

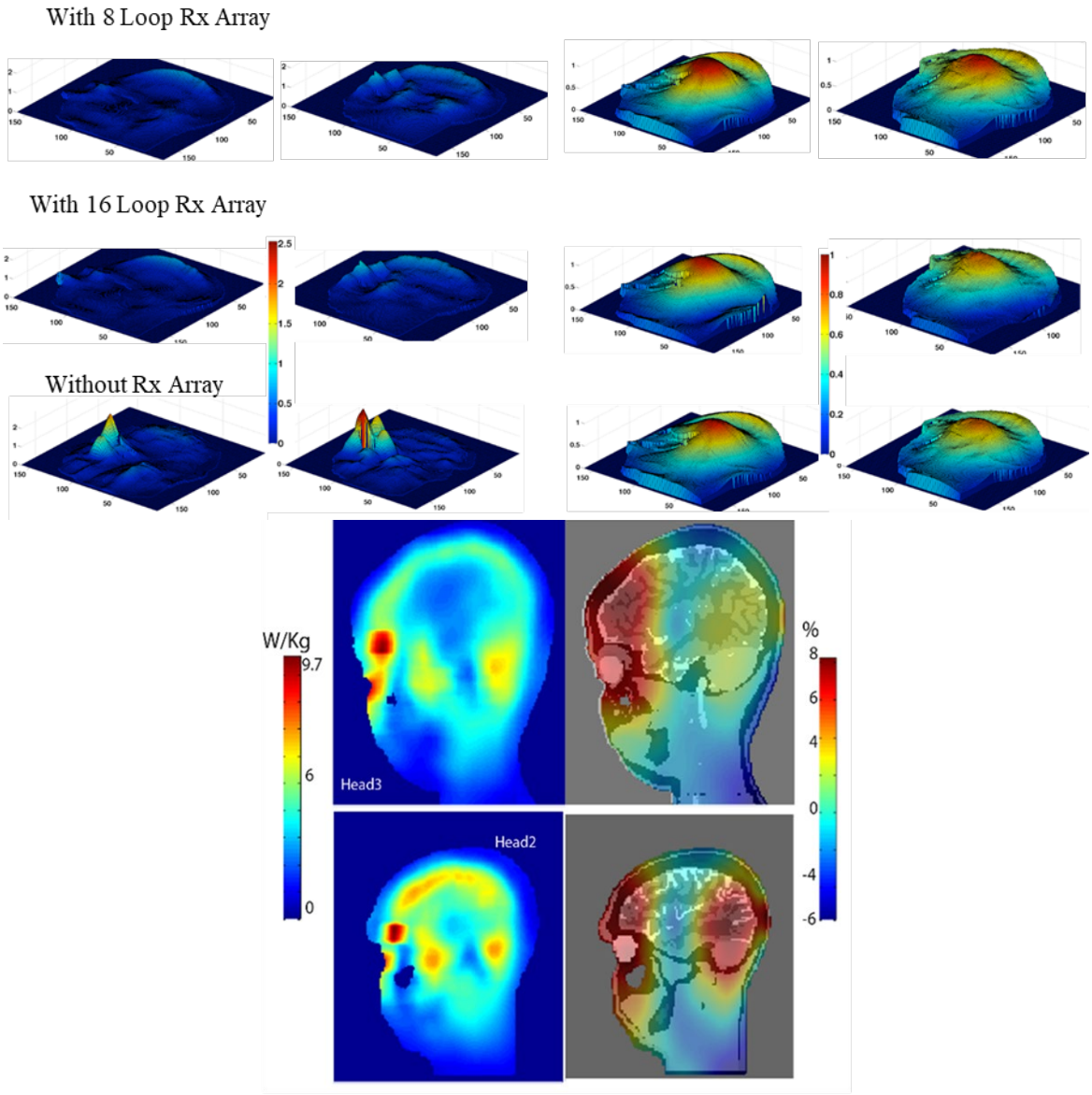

Figure 8: Changes in SAR - top: matching slices showing the effects of 8 and 16 cylindrical arrays on SAR distribution changes. bottom: Difference plots of SAR (W/kg per 10 g for 2 μT B_1^+in brain) distribution in the presence of different Rx-only inserts. Bottom figure: left column shows the SAR in the head without the Rx-only inserts and right column: the changes in SAR with Rx-only inserts. figure shows percent change in SAR with an 8-loop cylindrical Rx-only insert. Eyes and tissue adjoining sinuses and boundaries of tissues like CSF, bone, and GM show notable increase in absorption, from overlaid tissue conductivity plot of percent change in SAR. SAR hot spot changes in intensity with the inserts were observed, while some hot-spots intensity increased, others changed marginally or decreased

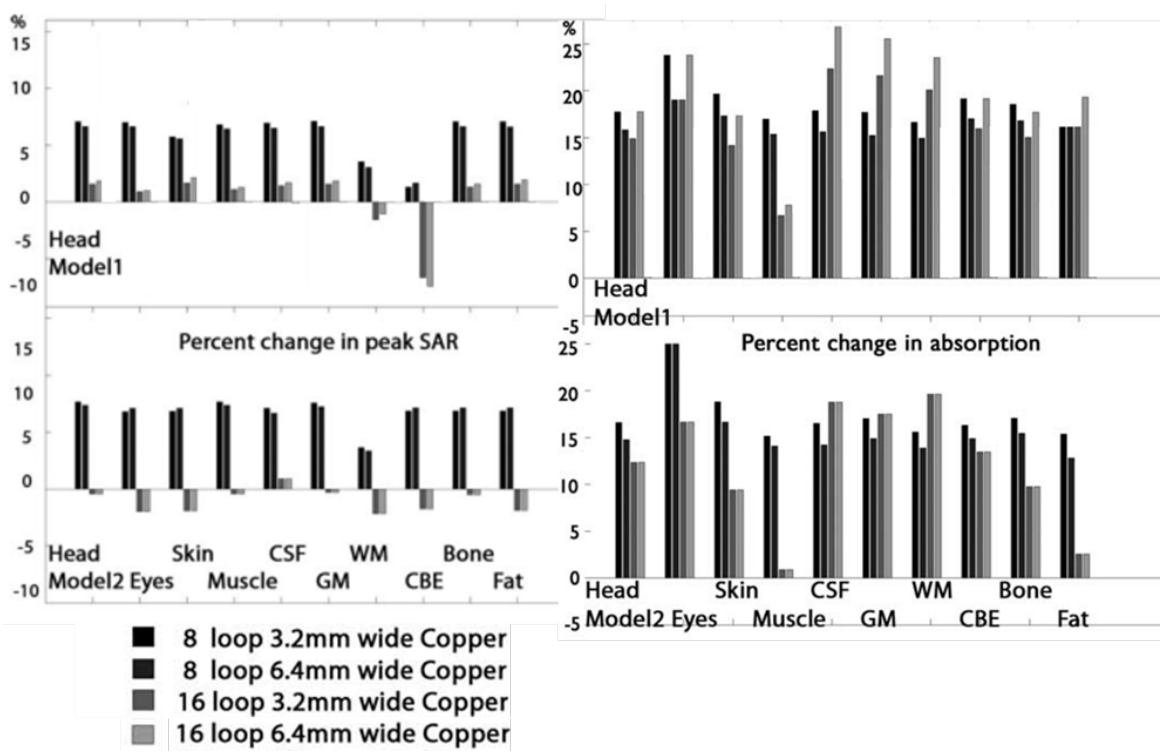

Figure 9: Change of global absorption and peak SAR intensity in the head models and nine tissues that constitute 80% of total absorption in the presence of different Rx-only inserts shown: Global absorption increase (9-18%) in the heads with Rx-only inserts; which indicate a change in RF radiation of the Tx coil even when changes in B_1^+ and coupling between ports of Tx coil were minimal. Peak SAR (hot-spot) locations and intensities in some tissues changed when different receive-only inserts were used. Change in peak SAR distribution was geometry dependent (> 8%) for the 8-loop array and did not change appreciably for the staggered 16-loop design. Effect of copper trace width on RF absorption is subtle, in some tissues, absorption increased for the staggered 16-loop array, while it decreased for the 8-loop array

3.1.4 Summary of Results

- Changing copper trace width of loops in array models caused subtle changes in RF absorption. SAR distribution changes were observed with Rx-only inserts.
- SAR hotspot intensity changes of -8 to +8% in different tissues for a mean B_1^+ in the brain of 2μ Tesla were observed with the Rx-only inserts, while some hot-spots intensity increased, others changed marginally or decreased.
- Global absorption increased (9-18%) for a mean B_1^+ in the brain of 2μ Tesla in the heads while it increased (14-21%) for 1 W forward power with Rx-only inserts; indicating a change in RF radiation of the Tx coil even when changes in B_1^+ and coupling between ports of Tx coil were minimal.
- Vulnerable structures like eyes & tissue adjoining sinuses and boundaries of tissues like CSF, Bone, and GM showed increase in absorption with the presence of Rx-only inserts.
- Peak SAR (hot-spot) locations and intensities in some tissues changed when different receive-only inserts were used. Change in peak SAR distribution was geometry dependent for the 8-loop array and did not change appreciably for the staggered 16-loop design.
- Effect of copper trace width on RF absorption is subtle, in some tissues, absorption increased for the staggered 8-loop array, while it decreased for the 16-loop array.

3.2 Effect of 32 Ch 16-18 AWG (1.3-1.1mm) Wire RX in TTT Coil

Current designs of loop arrays for ultra-high fields use 16-18AWG tinned wire with minimal copper coverage. Despite difficulties in constructing and modifying loop array using tinned wire (modifying overlaps and difficulties in building matching circuits); arrays built with wires reduce the transmit voltage required by 24 percent when compared with copper tape (13).

3.2.1 Effect of 32 Ch Rx Copper on Scatter Parameters and B_1^+

To test the effect of the close conforming 32 Rx array on the TTT transmit coil shown in Figure 10 and Appendix A1 (Figure 28). and, network analyzer measurements and corresponding FDTD calculations of TTT transmit coil without and with the detuned 32 Ch Rx array are performed and shown in Figure 11 and Table 5. In addition, FDTD statistical data for mean B_1^+ field calculated in the head is demonstrated in Table 5. The results show minimal changes in the B_1^+ field and SAR (not shown).

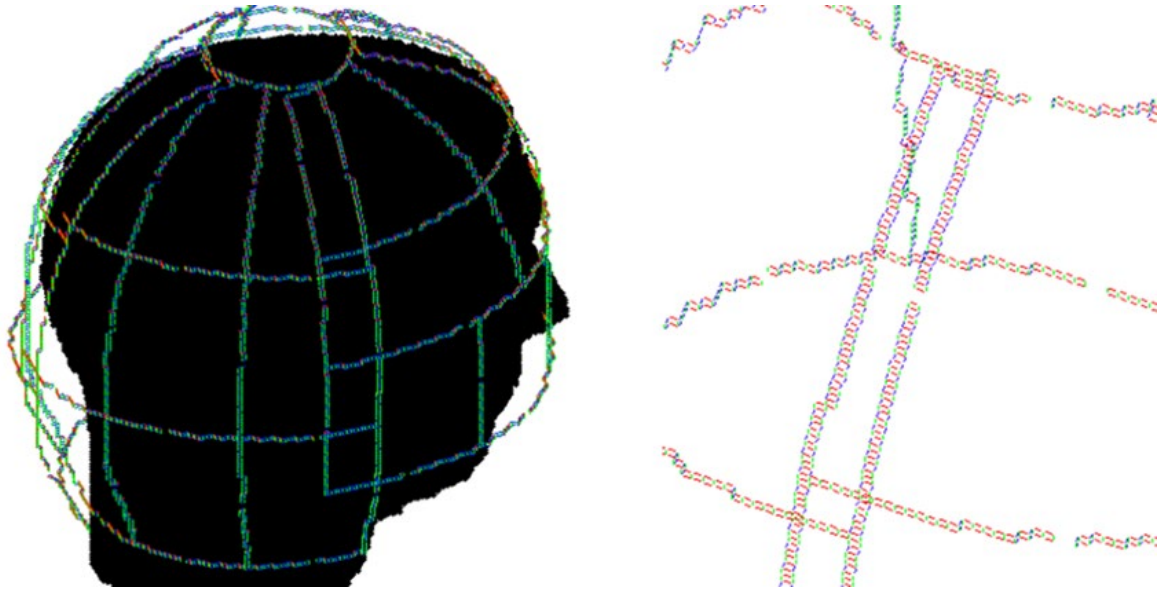

Figure 10: Extracted 32 Loop Array Geometry from CAD model of prototype (A1)

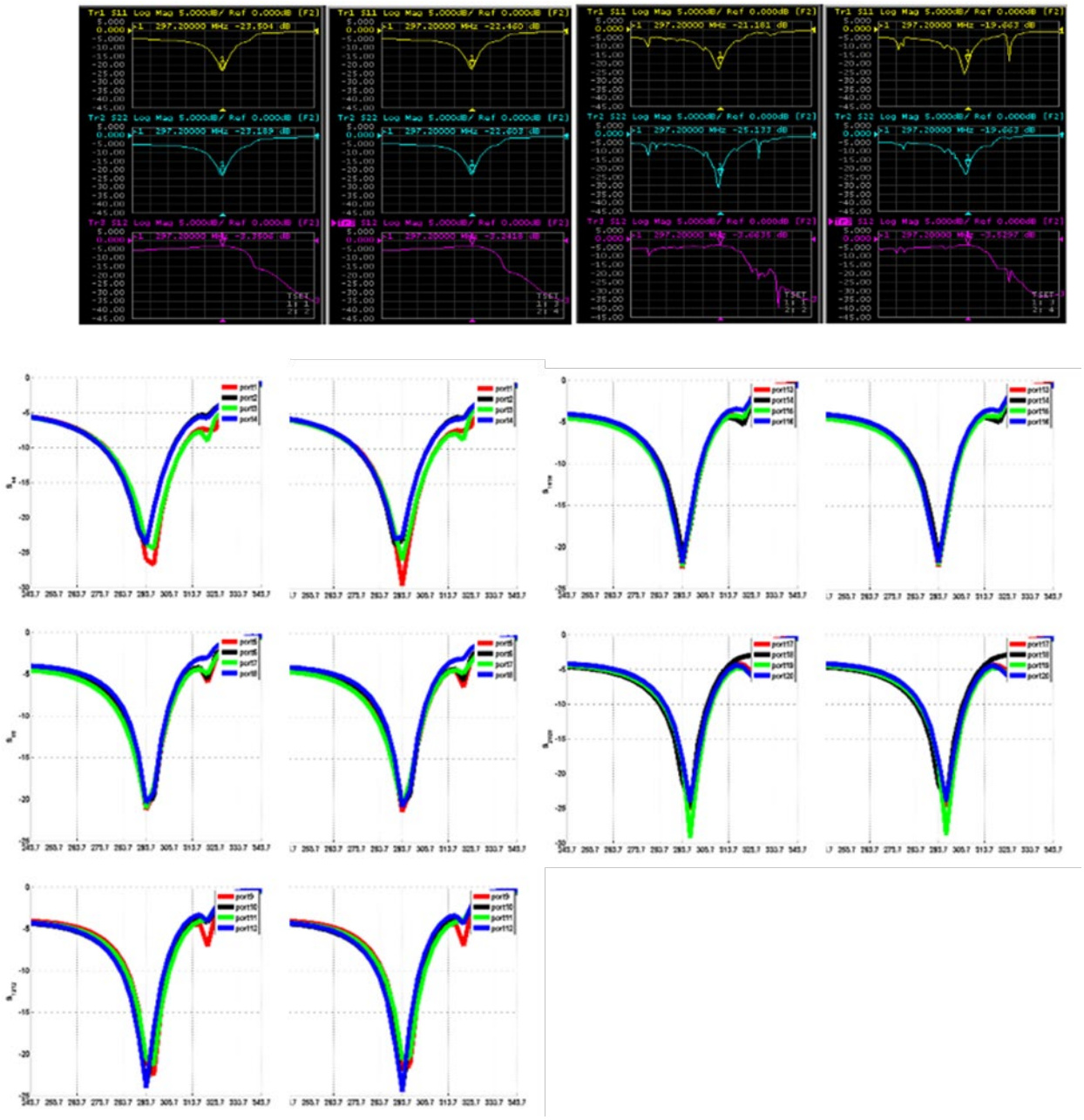

Figure 11: top: Network analyzer sample 4 ports of TTT Transmit Coil without/with 32 Ch Rx array. bottom: Scatter parameters from FDTD simulations of 20 Ch of TTT coil (left/right: without/with) detuned 32 Ch Rx loop array.

Table 5: FDTD calculated mean B_1^+ in head without and with detuned 32 ch Rx Array (16-18 AWG), Max % change in mean B_1 <11% with median mean B_1 change < 3%; thus the TTT transmit coil field in terms of mean B_1^+ did not change appreciably in the presence of the 32 Ch, Rx copper.

Port of TTT	bField Head only 1.0e+03	bField Head+Rx 1.0e+03	% change
1	1.52	1.66	-9.45
2	0.91	0.98	-7.93
3	1.70	1.76	-4.04
4	1.83	2.02	-10.41
5	1.40	1.44	-2.99
6	2.18	2.17	0.34
7	2.30	2.36	-2.59
8	1.59	1.61	-1.37
9	2.34	2.38	-1.70
10	1.48	1.53	-3.31
11	1.44	1.45	-0.49
12	2.61	2.66	-2.01
13	2.14	2.19	-2.30
14	1.97	1.98	-0.54
15	1.74	1.75	-0.58
16	1.92	1.97	-2.56
17	2.28	2.29	-0.41
18	1.65	1.67	-1.28
19	1.49	1.52	-2.05
20	1.72	1.75	-2.14

4.0 Phantom and In-vivo Benchmark Studies

4.1 Sperical Phantom Validation of Individual Channels of TTT Coil

Many phantom studies were done as part of safety assurance, and to obtain optimal excitation for the TTT coil developed in-house. Validating simulation and experiment of individual channels of TTT coil, a single-compartment spherical homogenous phantom (σ=0.46 S/m, ε =80) with 17.5 cm outer diameter was used to quantify B_1^+ field distribution from different channels of the coil model is compared with those obtained via. experimental B_1^+ mapping. The validation of the simulated B_1^+ field distribution with those acquired of all the transmit channels of the TTT coil developed in-house, enables us to obtain optimal RF shim parameters from FDTD simulations, which can be obtained for multiple heads and applied in-vivo without the need to shim per subject, during a clinical MRI.

Figure 12 shows the validation of B_1^+ field maps obtained via. FDTD simulations and those obtained experimentally in the Siemens 7T Magnetom.

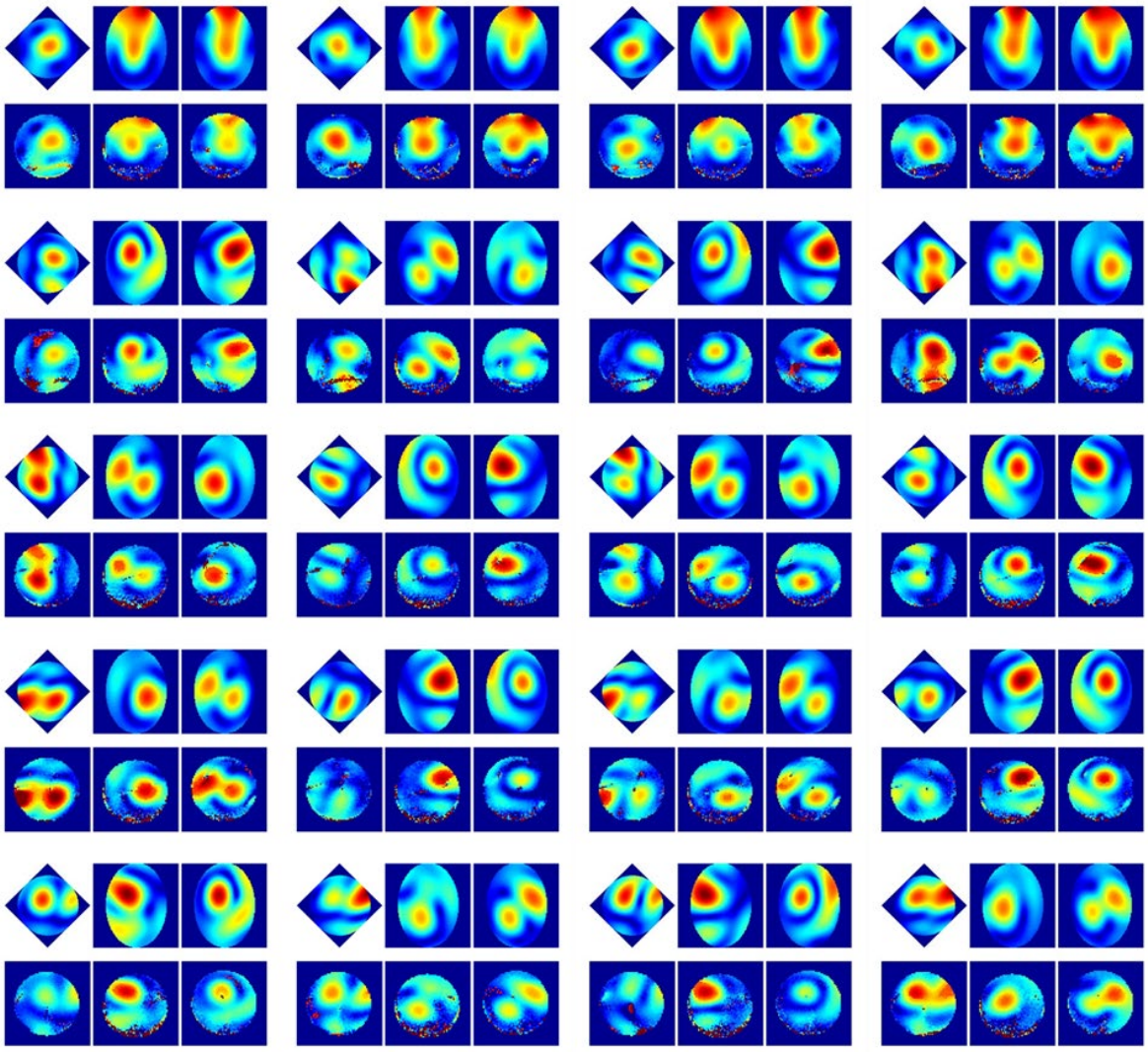

Figure 12: Shown are B_1^+ maps from numerical simulations (top sub- figure) and experimentally acquired B_1^+maps (bottom sub-figure). Note the simulation and experimental match of B_1^+ maps. the experimental maps were acquired in the PTX system with a Ref amplitude 1H 111V, measurements=6. The acquisition parameters: TR =2.2 sec, TE = 1.4 msec, FOV =220 mm, Matrix = 64x64, Thickness 3 mm, receiver bandwidth 510 Hz

4.2 Multi-Compartment Phantom Evaluation of Transmit Field Consistency

In this study, we quantify the transmit field consistency of a single-sided 4 channel Tic-Tac-Toe (4Ch TTT) head coil with commercially available 8 channel loop array (8Ch D) and birdcage (BC) head coils.

4.2.1 Methods

A 7-compartment phantom was used to quantify RF field consistency of the 7T head coils due to changes in RF loading. Mean B_1^+ intensity/distribution in 2D from head-to-foot slices were obtained for the different coils. As part of RF safety assessment, temperature rise to RF alone were measured in phantoms using fiber optic probes. Additionally, In-vivo experiments were done to demonstrate RF shimming for localized excitation and reception, using simulated fields without acquiring experimental field maps.

To evaluate the transmit B_1^+ field consistency, temperature rise and scattering parameters, a 7-compartment brain phantom with a volume = 1.75L was created. The benchmark phantom has the same constitutive properties (conductivity, dielectric constant) of an average brain at 300 MHz (σ=0.46 S/m, ε =80). Saline, ethanol and mineral oil mixtures doped with 10mM CuS04 (added to shorten T1 longitudinal relaxation) were used. An Oakton CON 110 conductivity meter (41) and a Dielectric Assessment Kit (DAK) system (42) were used to measure the conductivity and the dielectric constant of the different phantom liquids (Figure 13). Different doped saline and alcohol solutions with mineral oil were used to create varying dielectric constants and conductivities resembling different tissues. The description of the content of the 7-compartment phantom is shown in Figure 14 and its caption. Note that the stability of phantom liquids over

time (mixing homogeneity, lack of separation of phases and stability of composition etc.) was critical in performing the study.

Figure 13: Measurement of conductivity of Saline (25, 50, 80, 120 mM) doped with CuS04 to shorten T1 relaxation time using an Oakton 110 meter, 0.1 mho/m (S) = 1m mho /cm

The phantoms were positioned in the coils as per alignment of human subjects in clinical studies i.e. close to the coil element for the 4Ch TTT coil and in the middle of the 8 Ch D and BC coils. These settings represent actual alignment of human head (optimal for each coil) inside each coil. Figure 14 shows the alignment of the 7-compartment phantom inside each coil.

4.2.2 Experimental B_1^+ Field Mapping

B_1^+ field maps were obtained using a stimulated echo (STE: α-α-β, FOV =250 mm, 64x64 resolution, slice thickness 8 mm, band width per pixel 510 Hz, TR/TE =4/8m Sec) sequence. 8 slice intensity maps with 32 incremental voltages were achieved. The STE intensity is proportional

to sin2(α). Read out images of the incremental voltages were fit with a sin2 function with two parameters, namely the amplitude and frequency (x1 & x2). Intensity = x1*sin2(x2*pi*voltage). The x2 frequency parameter is proportional to magnitude of transmit B1+ field. Percentage differences in the B_1^+ field distributions in 8 axial slices inside the 7-comparmtment phantoms. Across all phantoms and slices except for one, the 4Ch TTT coil excites the most consistent B_1^+ field distributions/intensities followed by the 8Ch D coil.

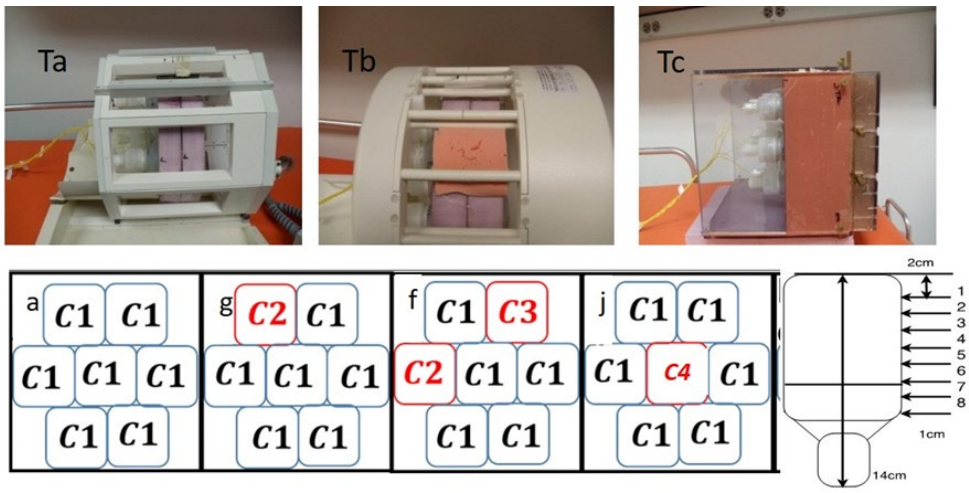

C1 (σ=0.46 S/m, ε =80) 50mM Saline +10mM CuSO4
C2 (σ=0.61 S/m, ε =80) 60mM Saline +10mM CuSO4
C3 (σ=0.76 S/m, ε =80) 75mM Saline +10mM CuSO4
C4 (σ=0.44 S/m, ε =50) , Ethanol 50% + 50mM Saline +10mM CuSO4

Figure 14: Top (pictures): (Ta) and (Tb) represent Rapid Biomedical 8-Channel decoupled array (8Ch D) and Invivo birdcage (BC) 7T head coils loaded with the same 7-compartment phantom, respectively. (Tc) represent a single-sided 4-channels Tic-Tac-Toe (4Ch TTT) coil loaded with 7-compartment phantom (bottom row: a-j) with a total volume 1.75L (250cc each). The XYZ-middle of the phantom was aligned with the XYZ-middle of the 8Ch D and BC coils. The XY-middle of the phantom was aligned with XY-middle of the 4Ch TTT coil and Z-top of the phantom was ½ inch away from the 4Ch TTT coil elements (Ta and Tb). These settings represent actual alignment (optimal for each coil) of the human head inside each coil. Bottom (diagrams): (a-j) represent 4 variations of the 7-compartment phantom. (a) represents the 7-compartment phantom with the same solution in each compartment [average constitutive properties (conductivity, dielectric constant) of brain (σ=0.46 S/m, ε =80)]. Different saline ethanol mixtures (doped with 10mM CuS04 to shorten longitudinal relaxation T1) and mineral oil were used to make constitutive properties similar to different tissues of the brain. (a): Homogenous brain phantom; (g): top left compartment substituted with liquid resembling grey matter (GM); (f): two compartments (left & top right) were substituted with liquid resembling GM and muscle respectively; (j) central compartment was substituted with liquid resembling muscle.

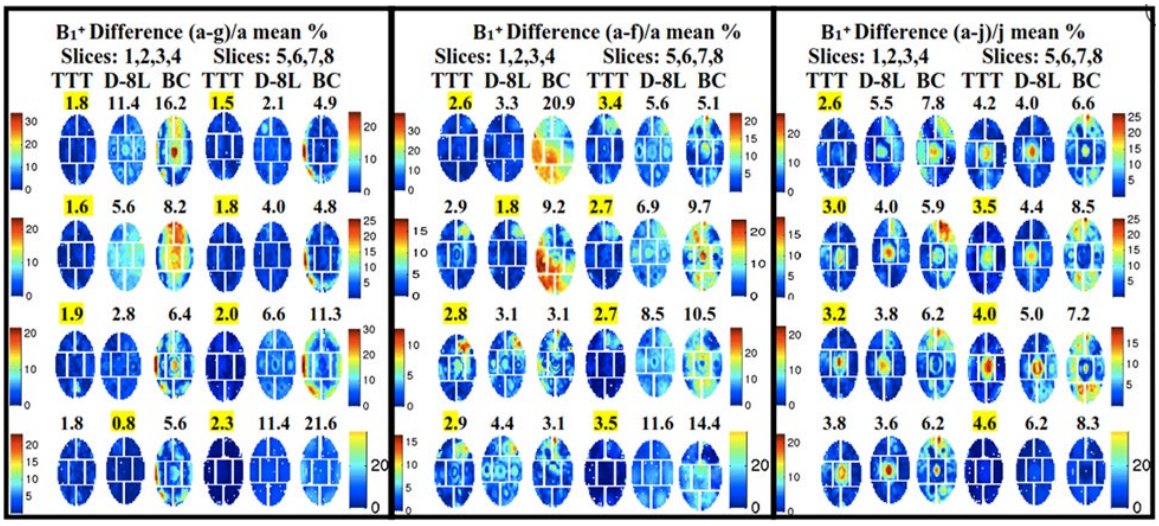

Figure 15: Percentage differences in the B_1^+ field distributions in 8 axial slices inside the 7-comparmtment phantoms. The percentage difference is calculated between original case (Phantom a in Figure 14) and new cases (Phantoms g, f and j were chosen as representative cases). The values above each sub-figure represent the average of the B_1^+ field percentage difference across the slice of interest. The positioning of the phantoms within each coil is described in Figure 14. The top 2cm of each phantom is excluded. The remaining 8 slices are spaced by 1cm. The highlighted cases represent consistency in performance, i.e. mean change of the B_1^+ field distribution out-performed the other two coils by at least 10%.

4.2.3 Results of Multi-Compartment Phantom Studies

The 4Ch TTT provides the most consistent transmit field of the two coils followed by the 8Ch D coil (43). Flip angle maps for a fixed input voltage obtained on a spherical homogenous phantom indicates that the single-sided 4Ch TTT coil produces a higher excitation up to +7cm

from the top of the phantom before intensity drops off when compared to the 8Ch D and Birdcage coils (not shown). Validation of simulation and experimental result of transmit B_1^+. In-vivo RF shimming in presented in 4.3.2.2 using full wave simulated RF fields validates 1) the consistency of the TTT coil performance (Figure 15) and 2) the rigorous RF full wave modeling approach, specifically the transmission line modeling mechanism for excitation and reception.

4.3 Computational and Experimental Evaluation of the Tic-Tac-Toe RF Coil for 7Tesla MRI

4.3.1 Background

The 7 compartment phantom studies done in 4.2 to evaluate consistency of transmit B_1^+ fields to perturbation in constituent property of imaged sample, were a precursor to this study done on anatomically detailed head models comparing RF field consistency in-vivo and simulations at 7Tesla. Many studies have been done to evaluate coil performance and safety assurance at 7T. Wolf et.al. 2013 carried out a comprehensive study of different human body models at 7T using a 16-element band-pass Birdcage coil, to assess how much detail is needed to accurately predict local SAR. In addition to looking at current distributions and SAR in different models, the paper compared local SAR hotspots in Duke (male) and Ella (female) virtual family models. Wang et.al. (44) compared B_1^+ homogeneity and SAR in a sphere at 7T for a 16-element birdcage, transverse electromagnetic resonator (TEM) and microstrip coils. The results showed that the B_1^+ homogeneity in the central axial plane of the sphere in the TEM coil was most homogeneous, with marginal difference in B_1^+ inhomogeneity between the microstrip and birdcage coils.

In this study, we perform a detailed analysis of the designs of two distributed-circuit based RF coils: the transverse electromagnetic resonator (TEM) head coil (36, 45) and the Tic-Tac-Toe (TTT) head coil (46-51) on multiple anatomically detailed head models and in-vivo. Bench measurements of s-parameters and experimental B_1^+ field distribution were obtained in volunteers and compared with numerical simulations. RF absorption, quantified by both average and peak SAR, and B_1^+ field intensity and homogeneity, calculated/measured in terms of maximum over minimum and coefficient of variation (CV) in the region of interest (ROI), are presented for both coils. RF consistency of both coils across multiple head models for different RF excitation strategies is also presented. While many electromagnetic simulation tools are currently used to calculate estimates of SAR for RF shimming purposes (52, 53), B_1^+ fields are typically experimentally measured/mapped in an experimental setting. In this study we compare 3 different RF shim for the two coils.

4.3.2 Methods

4.3.2.1 Anatomical Head Models

Five anatomically detailed head models (H1-5) were created from Duke male model of the Virtual family head models (54) (age: 34, height: 1.74 m, weight: 70 kg, body mass index (BMI): 23.1 kg/m2). The 22 tissue volumes, identified by its constitutive properties - conductivity and dielectric constant (σ, εr) - of the different head models are shown in Table 6. The head models were created by morphing the base model (H2) to produce models (H1-5) that varied in shape/eccentricity and volume and weights. The max variation in the weight was 14% and changes in shape was quantified by eccentricity of the head. The eccentricity measure is defined as the ratio of major to minor axis at the eye brow level. Eccentricity of heads varied from circular

(eccentricity ~ 1) to elliptical (eccentricity ~ 1.4). Figure 16 shows the contours of the different head models and their alignment in the TTT FDTD coil model (same top of head and back of head, in the coil as in an in-vivo MRI acquisition).

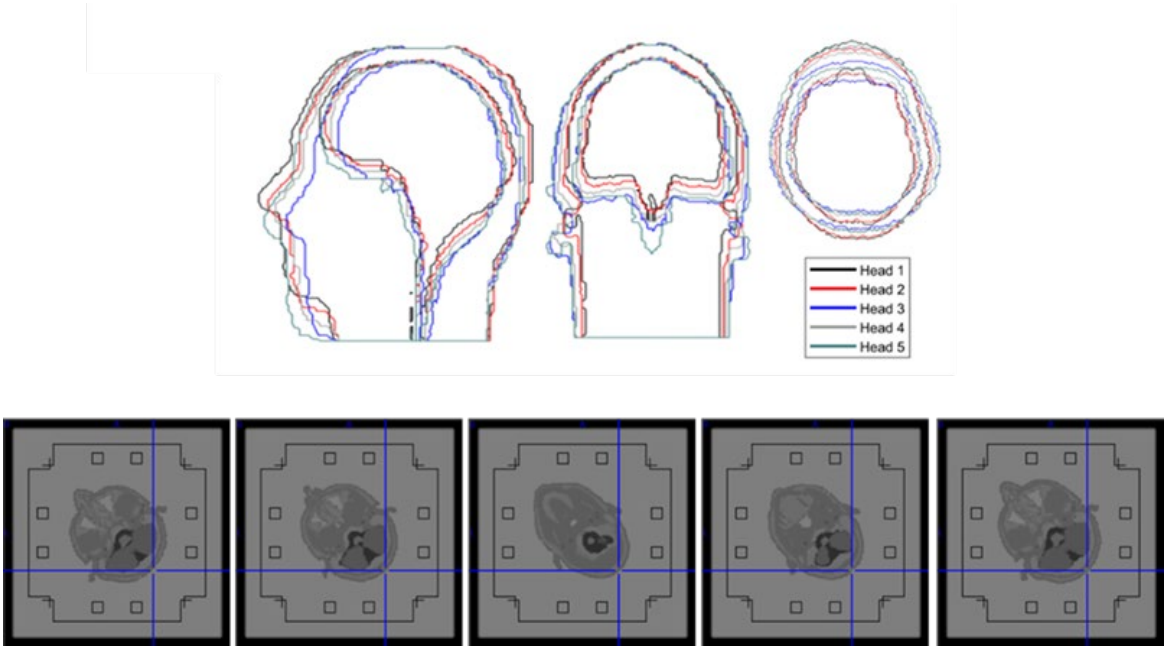

Figure 16: Contours of five anatomically detailed head models, bottom: head alignment in the TTT FDTD model all heads were aligned with the same top of head and back of head in the coils used as in an in-vivo MRI.

Table 6: Anatomically detailed head models. The 22 tissue volumes, identified by their constitutive properties (conductivity and dielectric constants) (σ, ε_r) of the different head models H1-5, are shown. The anatomically detailed head models H1-5 were created by morphing the Duke male model (H2) of the Virtual family head models (34). Models are arranged in increasing volume/weight.

Epsilon	Sigma	H1	H2	H3	H4	H5
5.64	0.04	126.5	131.6	143.0	141.4	160.9
5.76	0.03	514.6	503.9	475.0	493.2	529.4
13.45	0.08	561.6	582.2	617.5	612.6	690.1
26.82	0.29	169.8	174.3	189.6	186.3	211.2
36.95	0.42	444.8	472.3	507.5	492.7	566.1
43.82	0.41	17.7	15.0	10.8	13.2	12.1
46.81	0.55	33.0	26.9	18.5	21.7	21.1
48.00	0.54	30.7	24.6	19.2	22.2	21.1
48.97	0.65	29.3	29.9	32.6	31.2	36.4
49.90	0.64	42.6	40.6	35.6	36.6	40.4
51.96	0.55	404.1	404.1	401.7	404.7	443.4
51.96	0.63	0.2	0.2	0.3	0.3	0.3
58.23	0.77	529.2	547.6	588.1	580.5	659.1
58.93	0.74	110.0	114.6	124.4	118.9	139.3
58.93	0.97	998.8	974.2	905.1	954.0	1011.7
59.82	0.97	1.2	1.0	1.1	1.2	1.0
61.43	1.15	130.8	137.0	148.1	143.0	164.4
62.47	0.85	2.7	3.3	3.5	3.9	3.7
65.69	1.32	0.4	0.5	0.4	0.5	0.5
68.74	0.97	19.3	18.8	15.7	17.9	17.5
69.02	1.52	7.1	7.6	8.6	8.1	9.3
72.78	2.22	211.7	216.9	237.6	232.3	265.5
Dielectric Constant, and Conductivity		**4387**	**4427**	**4484**	**4516**	**5005**
		Individual Tissue Volumes and Total Volume (Cubic Cm) for each Head Model				

4.3.2.2 Muti-Head Shimming

Individual fields from different transmit ports of a coil were used as a composite volume comprising of the 5 head models. The shimming tool was used to obtain optimal shim (RF amplitude and phase for both the TEM and TTT coils). Three cases were chosen for both the coils:

1) quadrature (TEM) and pseudo-quadrature (TTT) excitation, and 2) RF shimming (optimized excitation using phase-only or amplitude-and-phase excitation) for both the TEM and TTT coils.

The RF shimming aims at achieving the lowest combination of the coefficient of variation (CV) and maximum to minimum (max/min) inside the region of interest (ROI) using a composite of the 5 head models. The ROI is the volume encapsulating the whole head above and including the temporal lobes and cerebellum while excluding the ears and the nasal cavity.

4.3.2.3 Coil Models

FDTD models of the TTT and TEM head coils i.e. the coil geometry: including the coaxial transmission lines, RF shielding, anatomically detailed head models and the terminating (perfectly matched layers) PML (55) are shown in Figure 17 and Figure 18. The 3-dimensional computational domains with isotropic resolution of ~1.6mm was constructed by setting the constitutive properties to that of the RF coil (comprising of Rexolite or, Teflon, or Copper) or to the different tissues of the anatomically detailed head models. The coil model has a true transmission line model for the excitation elements with accurate modeling capability of the coil's input impedance and coupling (40, 48, 56, 57).

The numerical models of the coils were tuned to Larmor frequency of 7T (297 MHz) using head model (H2) by adjusting the gap between the inner coaxial elements of the TTT and TEM elements and the modeling of the excitation source(s) while observing the scattering (S) matrix of

the true transmission line model. The same tuning configuration applied on H2 is utilized for all other head models without re-tuning/matching for each individual head model.

Note that the full wave 3D FDTD models of the TTT and the TEM coils and the generic framework of validating experiment with simulation studies of the transmit field, input impedance and coupling between coil elements have been performed and validated in earlier studies (40, 48, 57).

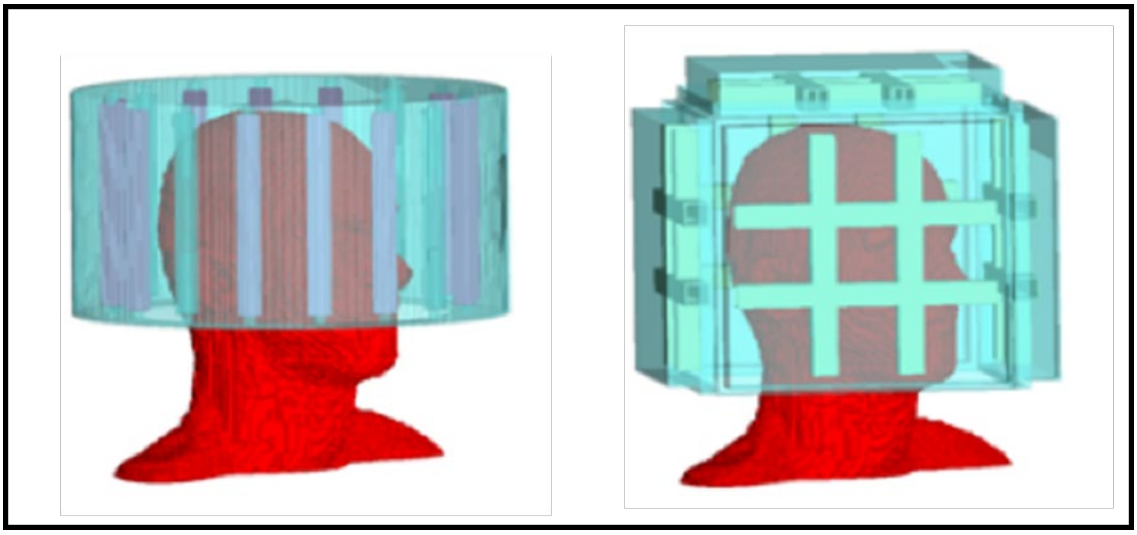

Figure 17: FDTD voxel models of Transverse Electromagnetic (TEM) and Tic-Tac-Toe (TTT) 7 Tesla head coils. The numerical models of the coils were tuned to Larmor frequency of 7T (297 MHz) using head model (H2) by adjusting the gap between the inner coaxial elements of the TTT and TEM elements and the modeling of the excitation source(s) while observing the scattering (S) matrix of the true transmission line model. Additional details regarding the full wave FDTD modeling domain in section 2.4.2 and Figure 2.

4.3.2.4 Excitation Strategy

The fields (electric and B_1^+) associated with the individual ports of each coil are combined using:1) quadrature (TEM) and pseudo-quadrature (TTT) excitation, and 2) RF shimming (optimized excitation using phase-only or amplitude-and-phase excitation) for both the TEM and

TTT coils. The RF shimming aims at achieving the lowest combination of the coefficient of variation (CV) and maximum to minimum (max/min) inside the region of interest (ROI) for all 5 head models. The ROI is the volume encapsulating the whole head above and including the temporal lobes and cerebellum while excluding the ears and the nasal cavity. The minimization of the CV and max/min inside the ROI is achieved by constraining the mean transmit B_1^+ field intensity to 11.74 μT, which results in 180^o flip angle with 1 ms square pulse, using a ~ 4.4 KW RF amplifier capacity (45% power loss from a standard 8 KW RF amplifier to the coil ports). Note that the phase-only shim cases (quadrature and phase-only arrangements) can be readily implemented in the combined mode of the MRI system without the need for parallel transmission mode.

RF absorption in the whole head quantified by SAR (W/Kg) averaged over any 10g of tissue was obtained for a continuous wave with mean transmit B_1^+ field intensity of 2μT in the ROI.

4.3.2.5 Coil Construction

Both the TTT and the TEM Tx coils use double-layered copper sheets (each layer is 4um 38.1 gram/m^2 Cu thickness with 0.254 mm dielectric between the layers.) For the TTT coil, the tic tac toe square-shaped array is made from (19.05 mm)^2 Polycarbonate dielectric with (6.35 mm)^2 inner opening for the inner rods (See). For the TEM coil, the elements are made of cylindrical-shaped (diameter = 12.7 mm) Teflon dielectric with inner opening (diameter = 6.35 mm) for the inner rods. The TEM elements are concentric with 279 mm diameter.

The excitation channels of each coil are combined using Wilkinson power dividers (2-, 4-, and 8- ways), with phase cables to implement particular RF shim phases (more on that in the "Excitation Strategy" section 4.3.2.4.)

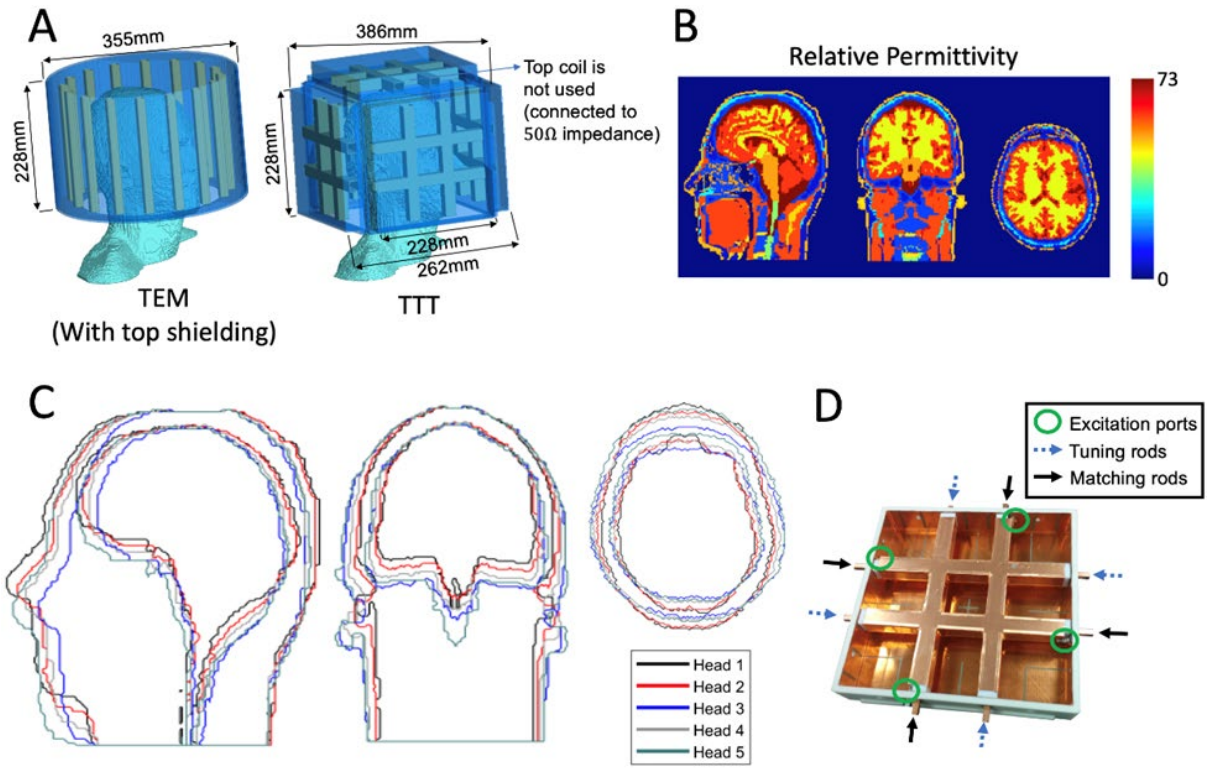

Figure 18: A) the TEM and TTT coil designs with anatomically detailed head model as the load; B) the relative permittivity maps of one of the head models; C) the superimposed outlines of all the head models; D) a constructed TTT coil side

4.3.2.6 Experimental Measurements -Network Analyzer and B_1^+ Field Mapping

Network Analyzer Measurements:

This study was approved by the University of Pittsburgh's Institutional Review Board (IRB PRO17030036) and involved four volunteers with approved written consent. The individuals have given a written informed consent to publish the details in this manuscript. Bench measurements were performed using a calibrated network analyzer (E5062A and 87050E multiport test set; Agilent Technologies Inc., CA, USA) together with an 85032B S-parameter test set. The Smith

Chart measurements of different excitation ports of the TTT and TEM coils were recorded for the four volunteers (without re-tuning/re-matching of the excitation ports between different heads). Thus, both measurements in-vivo on the four volunteers, and with the five head models (H1-5) in FDTD simulations, were obtained without re-tuning/re-matching of the excitation ports.

B_1 Mapping:

To achieve the desired phase shifts, the quadrature (for TEM) and pseudo-quadrature (for TTT) cases were implemented by adjusting the lengths of the coaxial cables feeding the coils. Imaging was performed on two volunteers using a 7T scanner (Siemens Medical Solutions, Germany). B_1^+ maps were acquired with a turbo FLASH sequence with the following parameters: number of flip angles = 6, TR = 2.2 sec, TE = 1.4 msec, FOV =220 mm, Matrix = 64x64, slice thickness = 3.2 mm and bandwidth = 510 Hz/pixel. The images from the six measurements of the B_1^+ map sequence was summed and used to create a brain mask. FSL's brain extraction tool (BET) (58) was used to create a brain mask (bet -m -f 0.4 options were used). The created brain masks were visually inspected and corrected manually using ITK SNAP tool (59) in the regions where automatic segmentation of the brain failed.

4.3.3 Performance Comparison of TEM and TTT Coils

4.3.3.1 Impedance and Network Analyzer Measurements

Figure 19 (A) and (B) show the FDTD calculated reflection coefficients (Sxx) and input impedances of different excitation ports in the TEM and TTT coils and the input impedances (real $\pm$ imaginary Ω) with the five head models (H1-H5). The displayed two (for the TEM coil) and four (for the TTT coil) reflection spectrums are representative of all the excitation channels of the TEM

and TTT coils. Figure 19 (C) also shows the bench measurements (using network analyzer) of the input impedances (Smith Chart) associated with two representative channels of the TEM and TTT coils on four different volunteers.

The numerical (across five different head models) and experimental (across four volunteers) results show that the reflection coefficient (Sxx) and input impedance values of both the TTT and TEM coils did not change appreciably. In terms of the input impedance, the maximum variation (between the five different head models) was 3.5% for the TEM coil (twenty cases represented by four excitation channels and five different head models) and 2.3% for TTT coil (eighty cases represented by sixteen excitation channels and five different head models.) The maximum variation measured with the network analyzer was 5%.

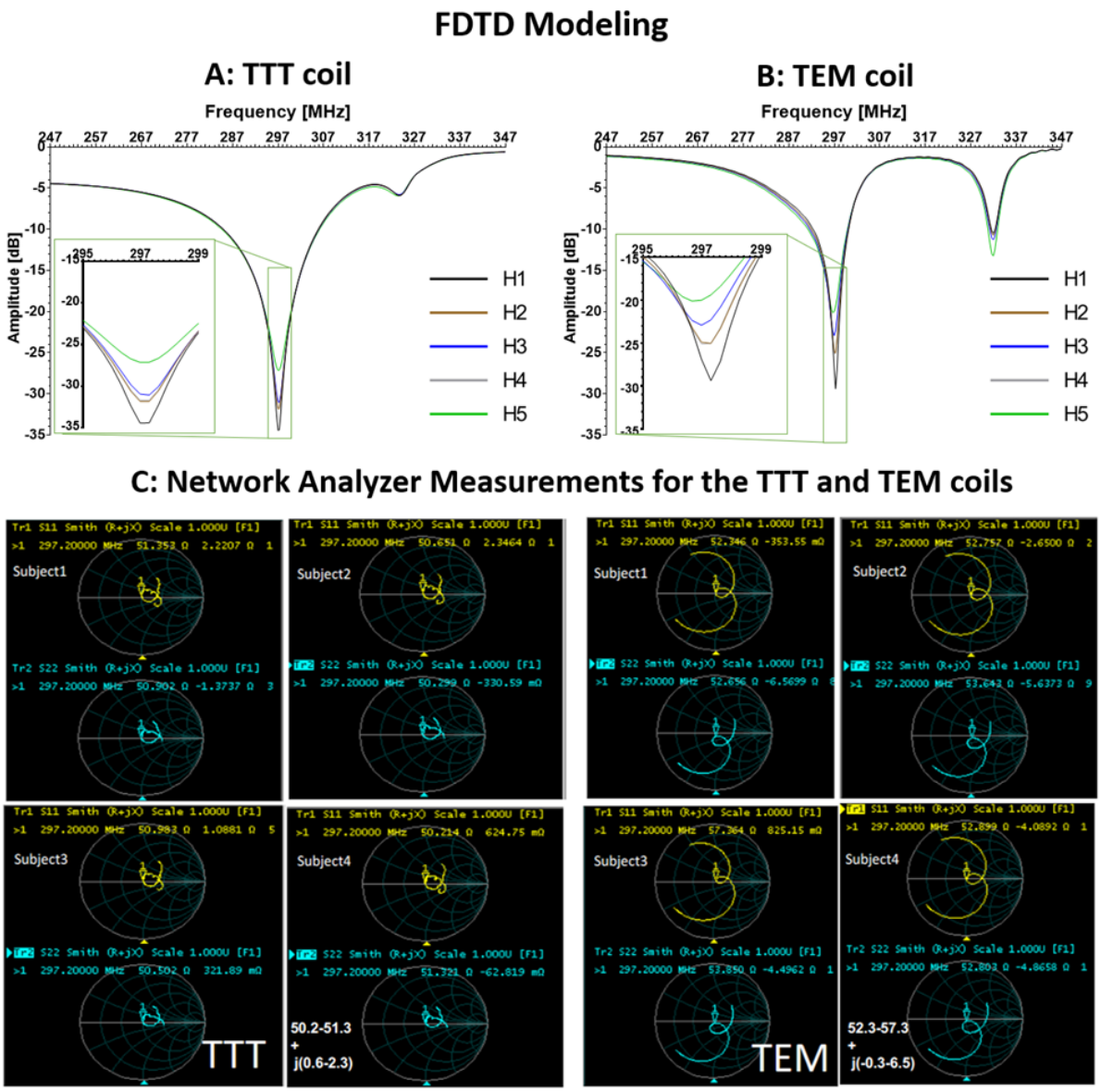

Figure 19: A) and (B) show the FDTD calculated reflection coefficients (Sxx) and input impedances of different excitation ports in the TEM and TTT coils and the input impedances (real ± imaginary Ω) with the five head models (H1-H5). The displayed two (for the TEM coil) and four (for the TTT coil) reflection spectrums are representative of all the excitation channels of the TEM and TTT coils. (C) also shows the bench measurements (using network analyzer) of the input impedances (Smith Chart) associated with two representative channels of the TEM and TTT coils on four different volunteers.

4.3.3.2 B_1^+ and SAR Distribution Comparison

Transmit B_1^+ field distributions across the five head models are shown for different excitation strategies Table 7 and Figure 20.

We compared three different excitation sets including quadrature, and variable amplitude-and-phase, and phase-only cases for the two coils. Due to the consistent tuning, and matching for both coils across different subjects, the coils were not re-tuned/matched in the simulations (five head models). FDTD Calculated stats for the B_1^+ field and SAR for the five head models summarised in Table 7 and Figure 20. B_1^+ field homogeneity is quantified in terms of max/min, and CV in the region of interest (ROI).

4.3.3.3 B_1^+ Homogeneity

Homogeneity of the B_1^+ field distribution was calculated in terms of maximum over minimum B_1^+ (max/min) and coefficient of variation (CV) which is defined as the standard deviation over mean ($\boldsymbol{\sigma}/\boldsymbol{\mu}$) in the ROI Figure 21.,Figure 22 , and Figure 23 show multiple axial, one coronal, and one sagittal slices of B_1^+ field distribution. Sagittal conductivity maps of the different head models are also plotted with a line indicating the end of cerebellum in each of the five head models. The ROI, where stats were obtained in the five head models (Table 7 and Figure 20) , includes the whole head above and including the cerebellum and excluding the nasal cavities and ears. The ROI volume of the different head models are different as indicated by the different axial slice number # which determines the end of cerebellum for each head model.

Table 7: Statistics for TEM and TTT coils for quadrature and pseudo-quadrature excitation, phase-only RF shimming, and phase-and-amplitude RF shimming. The average head model mass is 4.56kg (with 14% maximum variation among the models), the average brain volume is 1.51 L (with 15% maximum variation), and the average Eccentricity (major/minor axes) is 1.25 (with 37% maximum variation)

		B_1^+ Uniformity				Mean B_1^+ in the Same Volume (μT) for 1 W Input Power		Peak SAR over Average SAR		Average SAR (W/Kg) for Mean $B_1^+ = 2\mu$T in the Same Volume		Mean B_1^+ in the Same Volume over Sqrt(SAR) ($\mu T\sqrt{Kg}/\sqrt{W}$)	
		Maximum Intensity over Minimum Intensity in Whole Head above & Including Cerebellum and Excluding Nasal Cavity (Max B_1^+/Min B_1^+)		Standard Deviation over Mean in the Same Volume (CV)									
		TTT	TEM	TTT	TEM	TTT	TEM	TTT	TEM	TTT	TEM	TTT	TEM
Quadrature (TEM) and Pseudo-Quadrature (TTT)	Avg.	4.21	29.32	0.201	0.281	0.249	0.448	3.24	4.31	1.76	2.50	1.483	1.246
	Max Variation (%)	9.28	216.99	12.44	6.98	3.01	9.40	4.94	12.05	3.15	10.54	1.56	5.14
Phase-only RF Shimming	Avg.	3.97	7.94	0.197	0.266	0.247	0.451	3.24	4.58	1.87	2.40	1.441	1.271
	Max Variation (%)	10.29	44.54	10.47	7.46	2.99	9.83	6.26	13.60	4.48	10.37	2.21	5.06
Phase-and-Amplitude RF Shimming	Avg.	3.47	7.51	0.193	0.273	0.240	0.443	2.95	4.42	1.90	2.47	1.430	1.267
	Max Variation (%)	6.13	38.2	8.22	6.26	2.90	9.89	7.5	12.5	6.06	10.37	2.98	5.06

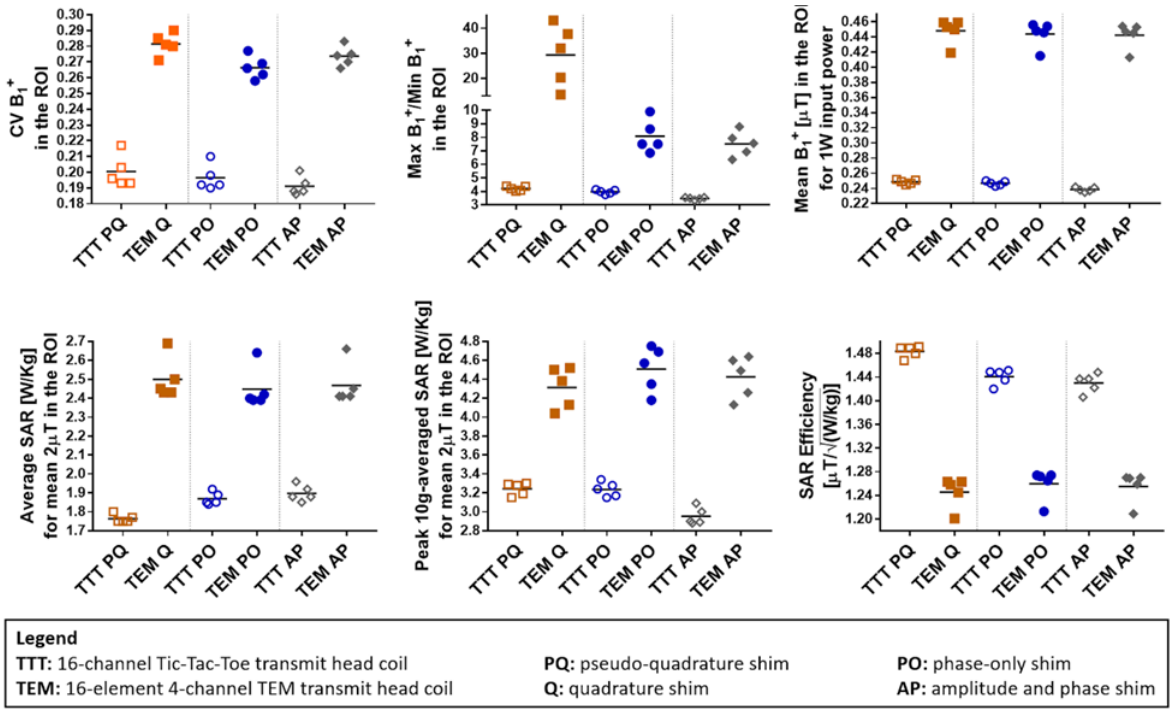

Figure 20: FDTD Calculated stats for the B_1^+ field and SAR for the five head models, and summarized in Table 7 are shown for the chosen RF shim cases. B_1^+ field homogeneity is quantified in terms of max/min, and CV in the region of interest (ROI). The ROI is defined as the whole head above and including the cerebellum and excluding the nasal cavities for all head models. The SAR performance is presented in terms of relationships between peak local SAR, average SAR, and B_1^+ field. Each line in each subfigure represents the mean value.

Table 7 and Figure 20 provides details of the following stats. In terms of quadrature (TEM) and pseudo-quadrature (TTT) excitation, the average (across H1-5) CV and max/min values for the B_1^+ field distribution are 20/28 % and 4.21/29.32 respectively for the TTT/TEM Coils. In terms of phase-only RF shimming, the average (across H1-5) CV and max/min values for the B_1^+ field distribution are 20/27 % and 3.97/7.94 respectively for the TTT/TEM Coils. In terms of amplitude-and-phase RF shimming, the average (across H1-5) CV and max/min values for the B_1^+ field distribution are 19/27% and 3.47/7.51 respectively for the TTT/TEM coils.

In terms of CV, the TTT design provides 40%/35%/41% average (across H1-H5) percentage improvement over the TEM design for quadrature/phase-only/amplitude-and-phase-excitation strategies. In terms of max/min, the TTT design provides 597%/99%/116% average (across H1-H5) percentage improvement over the TEM design for quadrature/phase-only/amplitude-and-phase excitation strategies.

4.3.3.4 B_1^+ Field vs. Input Power and SAR

We evaluated B_1^+ field efficiency based on SAR as well as input power. Table 7 provides relevant statistical details. In terms of quadrature (TEM) and pseudo-quadrature (TTT) excitation, the average (across H1-5) mean B_1^+ field intensity for 1 W input power and mean B_1^+ field intensity (in ROI) for 1 W average SAR ($\mu T\sqrt{Kg}/\sqrt{W}$)) (in whole head volume) are 0.25/0.45 [$\mu T/\sqrt{W}$] and 1.48/1.25 [$\mu T\sqrt{Kg}/\sqrt{W}$], respectively for the TTT/TEM Coils. Therefore, the TTT design has ~44% lower average B_1^+ intensity for 1W input power and ~18% higher average B_1^+ for 1 W/kg average SAR for this case. In terms of phase-only RF shimming, the average (across H1-5) mean B_1^+ field intensity for 1 W input power and mean B_1^+ field intensity for 1 W average SAR are 0.25/0.45 [$\mu T/\sqrt{W}$] and 1.44/1.27 [$\mu T\sqrt{Kg}/\sqrt{W}$], respectively for the TTT/TEM coils.

Thus, the TTT design presents ~44% lower B_1^+ for 1W input power and ~13% higher B_1^+ for 1 W/kg average SAR for the phase-only cases. In terms of amplitude and phase RF shimming, the average (across H1-5) mean B_1^+ field intensity for 1 W input power and mean B_1^+ field intensity for 1 W average SAR are 0.24/0.44 [$\mu T/\sqrt{W}$] and 1.43/1.27 [$\mu T\sqrt{Kg}/\sqrt{W}$] respectively for the TTT/TEM coils. Therefore, the TTT presents ~45% lower B_1^+ for 1W input power and ~13% higher B_1^+ for 1 W/kg average SAR for the phase-and-amplitude RF shimming.

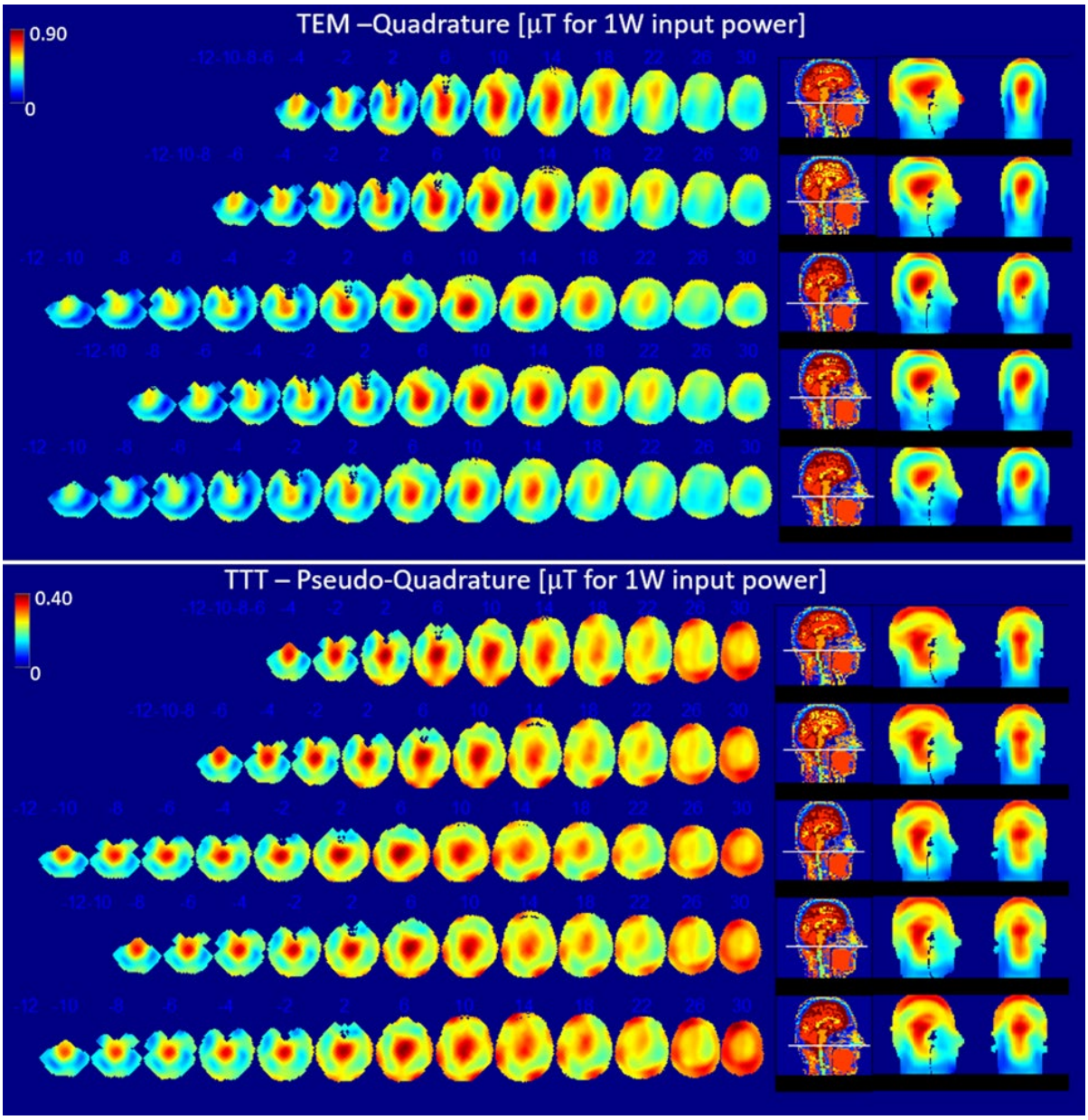

Figure 21: B_1^+ distribution for quadrature (TEM) and pseudo-quadrature (TTT) excitation: FDTD simulation data matching stats and conditions described in Table 7 and Figure 20. Axial slices were plotted with steps of 6.35 or 12.7 mm, slice numbers are indicated on top of each slice for instance (30, 26, ... 2, -2, -4, …-10 etc.). Slices are plotted every 6.35 mm from (slice -10) through (slice 2) to capture the end of cerebellum in the head model, and every 12.7 mm subsequently to visualize the B_1^+ field distribution for the five head models

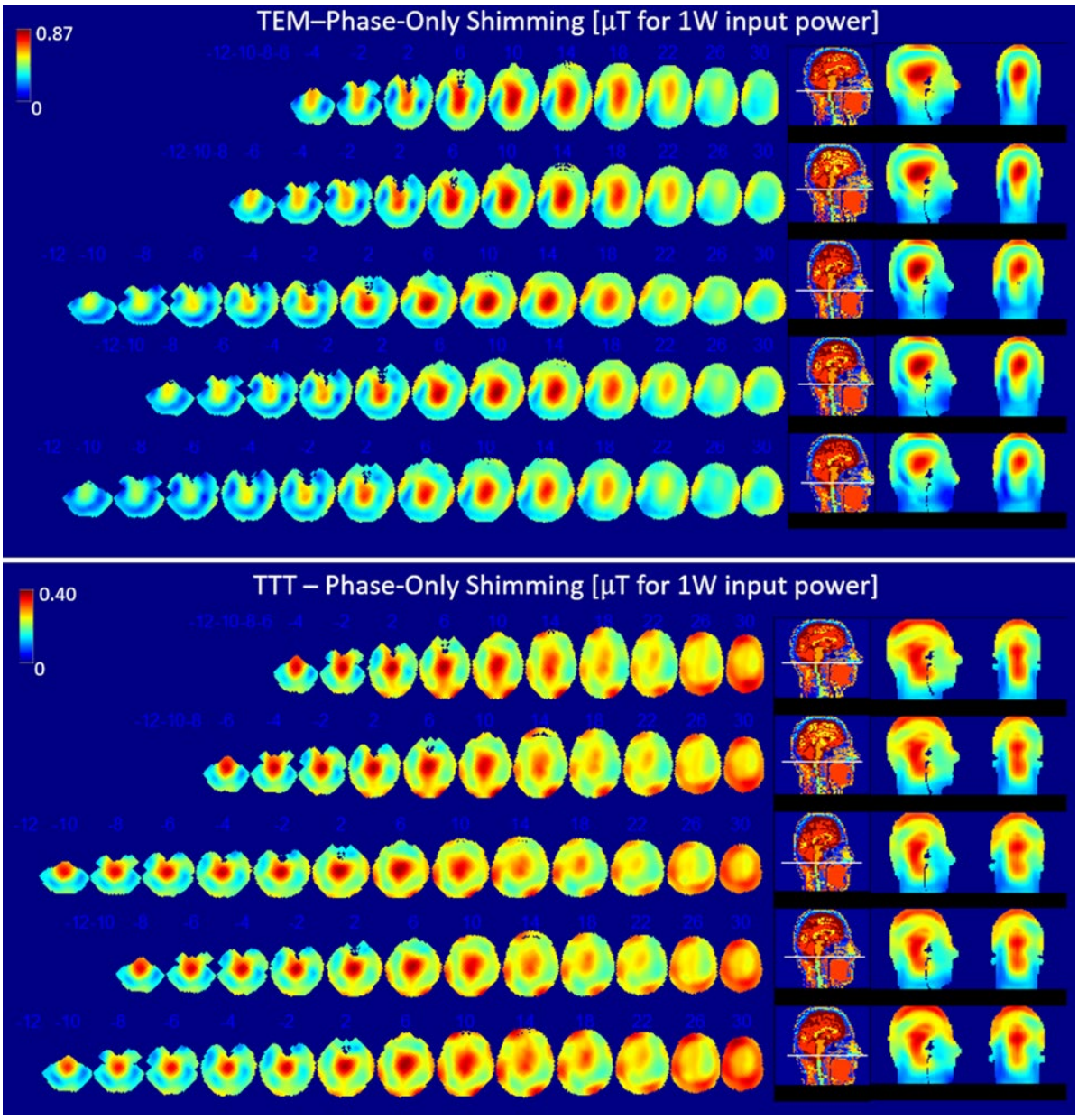

Figure 22: B_1^+ distribution for phase-only RF shimming: FDTD simulation data matching stats and conditions described in Table 7 and Figure 20.

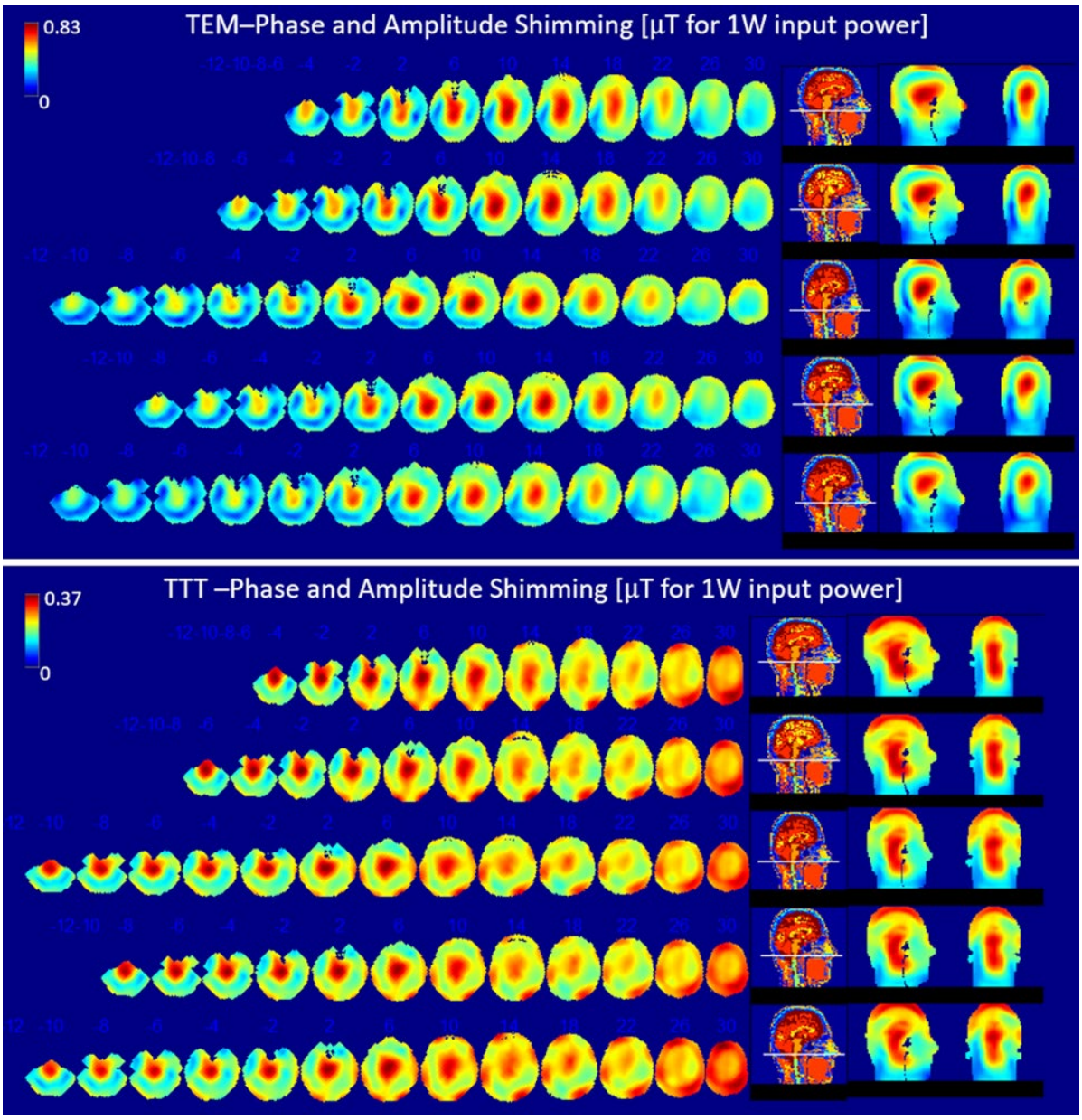

Figure 23: B_1^+ distribution for amplitude-and-phase RF shimming: FDTD simulation data matching stats and conditions described in Table 7 and Figure 20.

4.3.3.5 In-vivoB_1^+ Field Measurements

Consistent with the RF simulations, in-vivo measurements of transmit B_1^+ field distribution are shown below for the quadrature (TEM) and high flip angle pseudo-quadrature (TTT) excitation cases. The calculated CV for the TTT/TEM coils are ~21%/26% and ~20%/25% (Figure 24) respectively for the two subjects (note that the utilized phases/cable lengths were the same for both subjects). Lack of sufficient B_1^+ field intensity in parts of the temporal lobe and cerebellum by the TEM coil makes measurement and use of max/min criterion inaccurate, and therefore it was not measured.

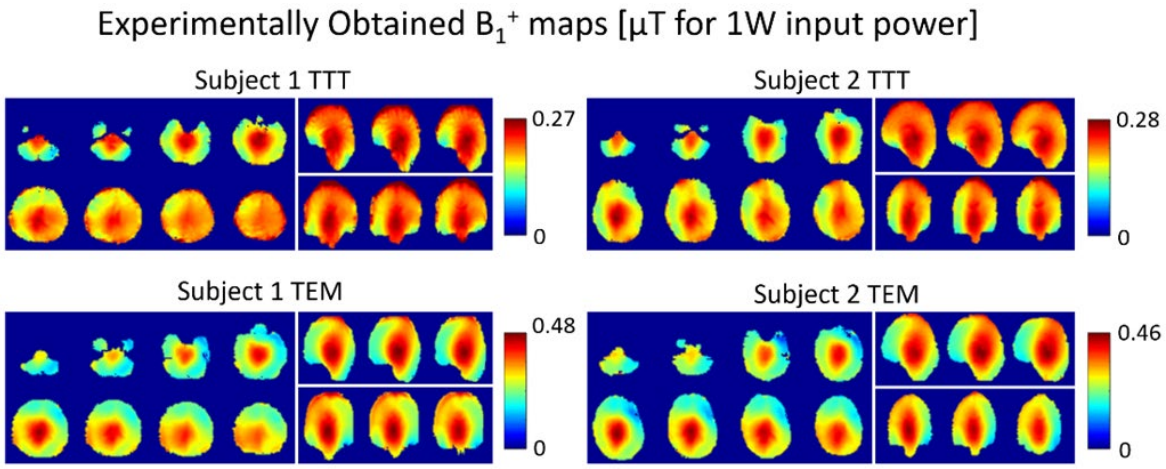

Figure 24: Experimentally obtained B_1^+ maps in two volunteers using the TEM and TTT coils. The color scale ranges from 0 to the maximum B_1^+ for each subject.

4.3.3.6 Numerical SAR Distribution

SAR distributions across the five head models are shown for the three different excitation strategies (Figure 25).

Average SAR

We evaluated SAR efficiency based on calculating average SAR (across the whole head volume) for 2μT mean B_1^+ field intensity in ROI. Table 7 and Figure 20 provide details of the following stats. In terms of quadrature (TEM) and pseudo-quadrature (TTT) excitation, the mean (across H1-5) average-SAR values for 2μT mean B_1^+ field intensity in ROI are 1.76/2.5 W/Kg for the TTT/TEM coils. In terms of phase-only RF shimming, the mean (across H1-5) average-SAR values for 2μT mean B_1^+ field intensity in ROI are 1.87/2.4 W/Kg respectively for the TTT/TEM coils. In terms of amplitude-and-phase RF shimming, the mean (across H1-5) average-SAR values for 2μT mean B_1^+ field intensity in ROI are 1.9/2.47 W/Kg respectively for the TTT/TEM coils. In terms of average-SAR values for continuous 2μT mean B_1^+ field intensity in ROI, the TTT design provides 30%/22%/23% lower average (across H1-H5) values when compared to the TEM design for quadrature/phase-only/amplitude-and-phase excitation strategies.

Local SAR

We evaluated SAR distribution based on calculating local SAR (W/Kg for 10 g) to average SAR (W/Kg for 10 g) ratio. Table 7 and Figure 20 provide details of the following stats. In terms of quadrature (TEM) and pseudo-quadrature (TTT) excitation, the mean (across H1-5) local to average SAR ratio are 3.2/4.3 respectively for the TTT/TEM coils. In terms of phase-only RF shimming, the mean (across H1-5) local to average SAR ratio are 3.2/4.6 respectively for the TTT/TEM Coils. In terms of amplitude-and-phase RF shimming, the mean (across H1-5 local to average SAR ratio are 2.9/4.4 respectively for the TTT/TEM Coils. In terms of local SAR to

average SAR ratio, the TTT design provides 25%/30%/34% lower average (across H1-H5) values when compared to the TEM design for quadrature/phase-only/amplitude-and-phase excitation strategies.

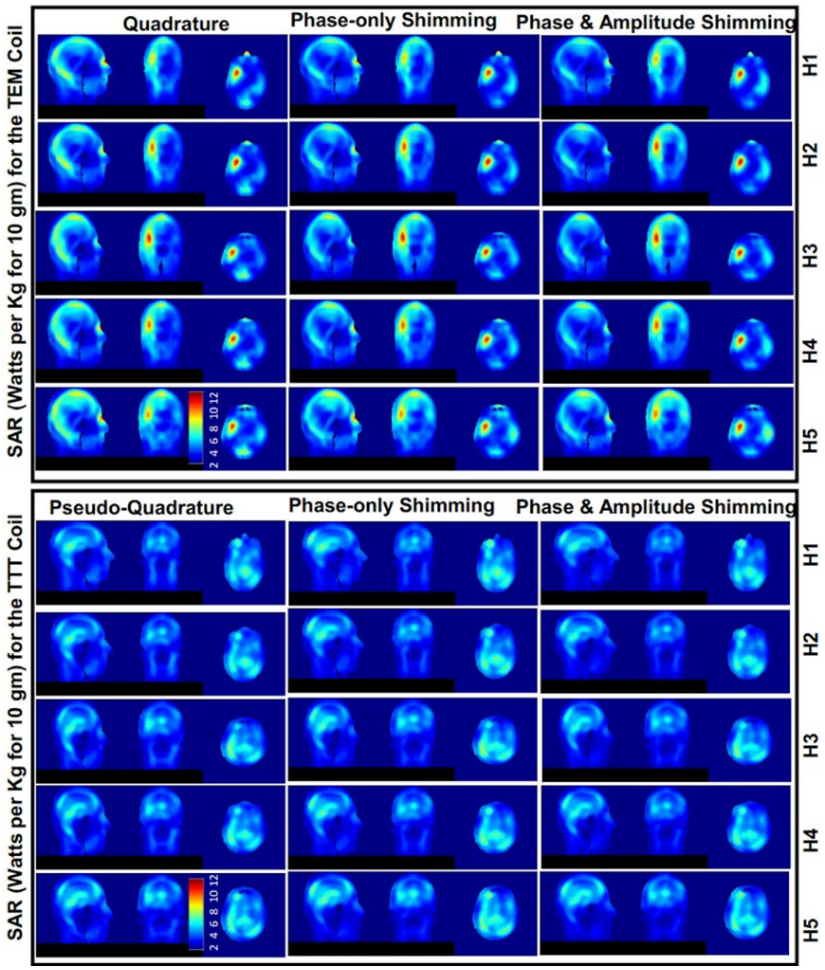

Figure 25: SAR (W/Kg for 10 g) distribution for 2μT mean B_1^+ in the ROI in all head models H1-5 in the TEM and TTT coils. Exemplar axial, sagittal, coronal slices of SAR are shown. The distributions are plotted to the same maximum of 12 W/Kg for 10 g. The SAR is plotted for pseudo-quadrature arrangement, phase-only RF shimming (one RF shim set for coil applied on all 5 head models), and amplitude-and-phase RF shimming (one RF shim set for coil applied on all 5 head models). Please see Table 7 and Figure 20 for the conditions under which the SAR distributions are plotted.

4.3.4 Consistency of RF Field Distributions

B_1^+ Field

We evaluated the consistency of B_1^+ field based on the four-abovementioned criteria namely: CV, max/min, mean B_1^+ field intensity for 1 W input power and mean B_1^+ field intensity for 1 W average SAR. B_1^+ field consistency was based on calculating the maximum variation change among the five head models, i.e. for any criteria, maximum variation is defined as [maximum value – minimum value] over [minimum value]. In terms of CV, the maximum variation change is 12/7%, 10/7.5%, and 8.2/6.3% respectively for the TTT/TEM coils and for quadrature, phase-only, and amplitude-and-phase excitation strategies, respectively. For max/min, the maximum variation change is 9.3/217%, 10/44%, and 6.1/38% respectively for the TTT/TEM coils and for the three excitation strategies. For mean B_1^+ field intensity for 1 W input power, the maximum variation change is 3/9.4%, 3/9.8%, and 2.9/9.9% respectively for the TTT/TEM coils and for the three excitation strategies. For mean B_1^+ field intensity for 1 W average SAR, the maximum variation change is 1.6/5.1%, 2.2/5%, and 3.0/5% respectively for the TTT/TEM coils and for the three excitation strategies.

SAR

We evaluated the consistency of SAR based on the two-abovementioned criteria namely average SAR (in whole head volume) for 2μT mean B_1^+ field intensity in ROI and local to average SAR ration. In terms of SAR (in whole head volume) for 2μT mean B_1^+ field intensity in ROI, the maximum variation change is 3.1/10%, 4.5/10%, and 4.5/10% respectively for the TTT/TEM coils for quadrature, phase-only, and phase-and-amplitude excitation strategies. For local to average SAR ratio, the maximum variation change is 4.9/12%, 6.3/14%, and 6/14% respectively for the TTT/TEM coils for the three excitation strategies.

4.3.5 Performance Comparison Summary

1) Both coils present negligible variance of input impedance among different head models/subjects (<5%) in the simulated/measured data.

2) The TTT design shows substantial improvement in the B_1^+ homogeneity and consistency demonstrated in the max/min values of the TTT design (mean max/min = 3.97, maximum variation = 10% between different heads) when compared with that achieved with the TEM design (mean max/min = 7.94, maximum variation = 44%), which represents a significant a) excitation drop in the cerebellum and temporal lobes and b) variation between subjects.

3) The TTT design presents substantial improvement in the B_1^+ homogeneity, as demonstrated in the values of the CV (TTT = 0.20 mean, 10% maximum variation between different heads; TEM = 0.27 mean, 7.5% maximum variation). This is critical for achieving fidelity of the B_1^+ field distribution across the human head. The TTT design has a significant lower B_1^+/power efficiency, with mean B_1^+ = 0.25μT for 1W input power (with 3.0% maximum variation) against 0.45μT (with 10% maximum variation) for the TEM design; however, both coils

present enough B_1^+ intensity to have spin inversion with 1ms square pulse and 8kW RF power amplifier including power losses. This could be critical when high peak B_1^+ intensity is needed with limited RF power amplifier capacity.

4) The TTT design has better SAR efficiency, with 1.44 μT/√(W/kg) (maximum variation = 2.2% between different heads) against 1.27 μT/√(W/kg) (maximum variation = 5.1%) for the TEM design. This is critical for high SAR acquisitions (turbo spin echo, FLAIR, DTI, etc...)

5) The TTT design has lower peak over average SAR ratio (3.24) with maximum variation = ~6.3% between different heads against 4.58 (which is ~41% higher than the TTT value) and maximum variation = ~14% for the TEM design. This is critical for high SAR acquisitions as well as meeting the regulatory limits for local and average SAR. Note that with the FDA-approved single transmit mode 7T systems, the scanner's online SAR calculations do not significantly change between different human heads.

For the TTT coil, the lack of significant variation in terms of B_1^+ distribution/intensity and local/average SAR in different subjects translates to ease in set up (no B_1^+ maps and RF shimming for every subject are necessary). This is very important in a clinical environment when the time to scan a subject is very limited and any retuning or extra acquisition is costly. Moreover, the subject-insensitivity RF performance associated with the TTT design provides greater RF safety assurance measured by consistency in the local and average SAR with different subjects. With narrow tolerance parameters associated with TTT coil, the results also show that numerical simulations can be potentially performed on a representative head model without the need for 1) subject-specific transmit B_1^+ maps measured in-vivo or 2) subject-specific SAR calculations. Finally, the TTT and TEM RF coils can be used in either parallel transmit or in single transmit systems.

5.0 Summary of Results

5.1 Effects of Cylindrical RX-inserts

- Changing copper trace width of loops in array models caused subtle changes in RF absorption. SAR distribution changes were observed with Rx-only inserts.
- SAR hotspot intensity changes of -8 to +8% in different tissues for a mean B_1^+ in the brain of 2μ Tesla were observed with the Rx-only inserts, while some hot-spots intensity increased, others changed marginally or decreased.
- Global absorption increased (9-18%) for a mean B_1^+ in the brain of 2μ Tesla in the heads while it increased (14-21%) for 1 W forward power with Rx-only inserts; indicating a change in RF radiation of the Tx coil even when changes in B_1^+ and coupling between ports of Tx coil were minimal.
- Peak SAR (hot-spot) locations and intensities in some tissues changed when different Rx-only inserts were used. Change in peak SAR distribution was geometry dependent (> 8%) for the 8-loop array and did not change appreciably for the staggered 16-loop design.
- Effect of copper trace width on RF absorption is subtle, in some tissues, absorption increased for the staggered 16-loop array, while it decreased for the 8-loop array.

5.2 Effects of 32 Ch RX-insert

While thicker copper traces (3.2 & 6.4 mm) of cylindrical Rx inserts showed changes in RF absorption in the TEM coil, the close conforming 32Ch helmet Rx array with 16-18 AWG (copper of 1.3-1.1mm diameter) did not alter the mean B_1^+ or tuning of individual channels of TTT transmit coil.

5.3 Benchmark Studies -Simulations and In-vivo

We evaluated the B_1^+ field produced in the ROI that encapsulates the whole head above and including the temporal lobes and cerebellum and excludes the nasal cavity, and SAR in the whole head volume for the TEM and TTT coils. Statistics of the simulated B_1^+ field (efficiency, homogeneity, and consistency), and SAR (intensity and consistency of average and local values) across the 5 head models.

1) Both coils present negligible variance of input impedance among different head models/subjects (<5%) in the simulated/measured data.

2) The TTT design shows substantial improvement in the B_1^+ homogeneity and consistency demonstrated in the max/min values of the TTT design (mean max/min = 3.97, maximum variation = 10% between different heads) when compared with that achieved with the TEM design (mean max/min = 7.94, maximum variation = 44%), which represents a significant a) excitation drop in the cerebellum and temporal lobes and b) variation between subjects.

3) The TTT design presents substantial improvement in the B_1^+ homogeneity, as demonstrated in the values of the CV (TTT = 0.20 mean, 10% maximum variation between

different heads; TEM = 0.27 mean, 7.5% maximum variation). This is critical for achieving fidelity of the B_1^+ field distribution across the human head. The TTT design has a significant lower B_1^+/power efficiency, with mean B_1^+ = 0.25μT for 1W input power (with 3.0% maximum variation) against 0.45μT (with 10% maximum variation) for the TEM design; however, both coils present enough B_1^+ intensity to have spin inversion with 1ms square pulse and 8kW RF power amplifier including power losses. This could be critical when high peak B_1^+ intensity is needed with limited RF power amplifier capacity.

4) The TTT design has better SAR efficiency, with 1.44 μT/√(W/kg) (maximum variation = 2.2% between different heads) against 1.27 μT/√(W/kg) (maximum variation = 5.1%) for the TEM design. This is critical for high SAR acquisitions (turbo spin echo, FLAIR, DTI, etc...)

5) The TTT design has lower peak over average SAR ratio (3.24) with maximum variation = ~6.3% between different heads against 4.58 (which is ~41% higher than the TTT value) and maximum variation = ~14% for the TEM design.

Appendix A Receive Design

Loop array sensitivity is maximum closest to the loop and falls off rapidly (11), thus we wanted to make a receive that conforms to the heads of different subjects.

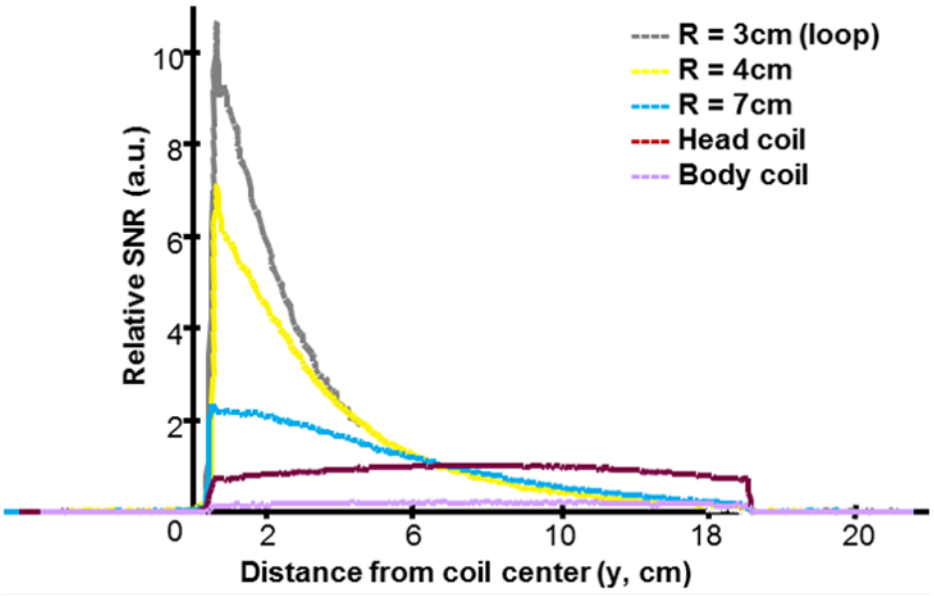

Figure 26: Rx sensitivity with distance from loop

A.1 Multi-part RX for 32 Ch Array

A multi-part receive could be adjusted to conform to different head shapes and sizes. We iterated designs comprising of 3-part receiver and settled on a 4-part receiver. The 4-parts of the receiver is adjustable to fit 90 percentile head sizes as per (60) and summarized in Table 8.

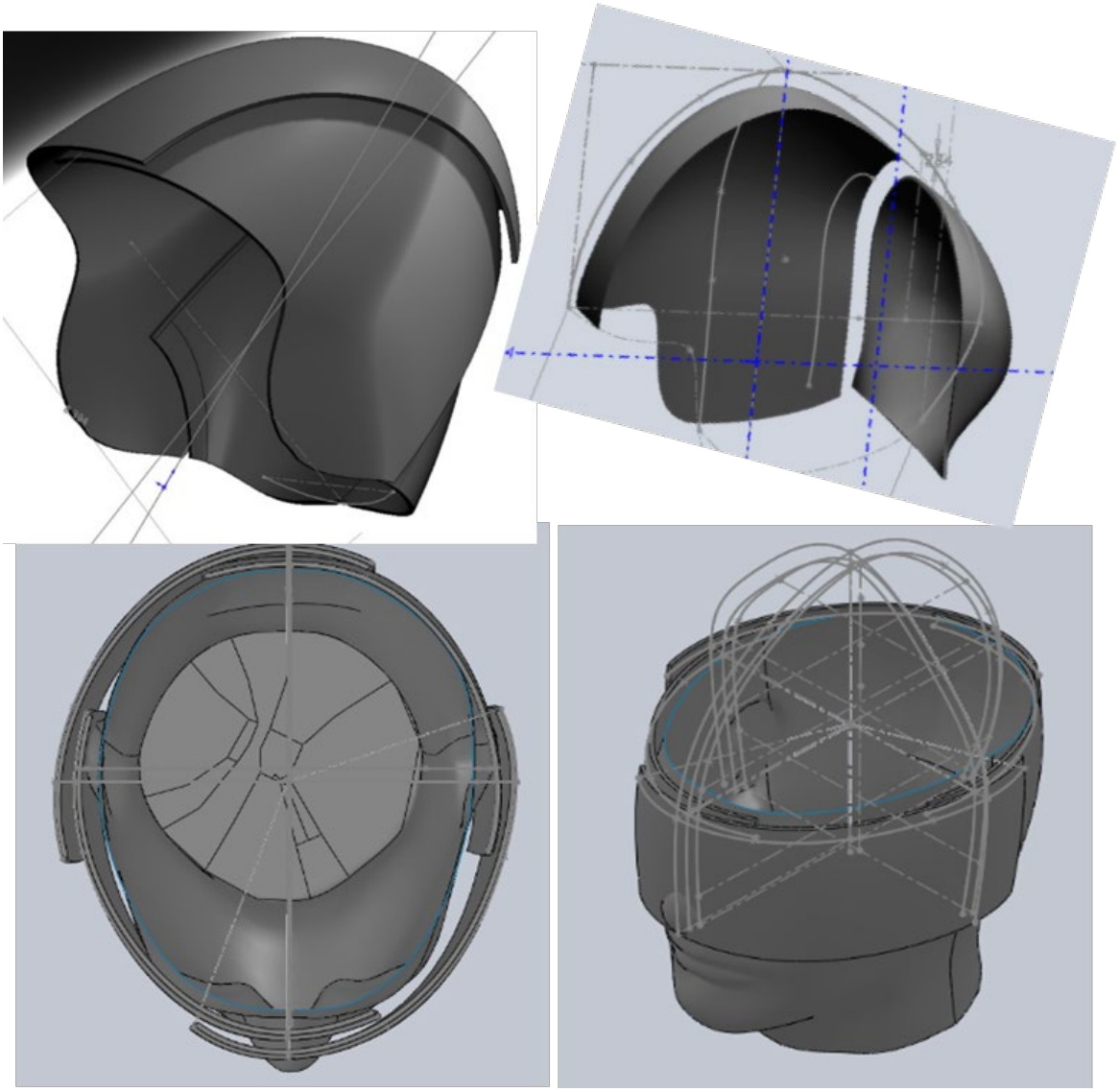

Figure 27: Multi-part Receive Designs that conforms the head: 3-part and 4-part overlapped receive designs

Table 8: Male and Female heads of typical North American population measurements were used (60), different heads were fit in the CAD models before the 4-piece receiver was 3d printed

	Length (min, mean, max) inches	Width (min, mean, max) inches
Male	7.1, 7.7, 8.4	5.6, 6.1, 6.7
Female	6.4, 7.1, 7.8	5.2, 5.7, 6.3

In-laid grid localizes loop geometry. Below: extracted loop array copper geometry for RF simulations, copper of detuned 32 RX-array was used to verify its effect on TX-Coil fields

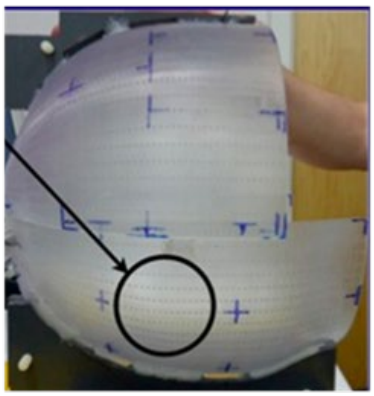

Figure 28: Prototyped Tx-Coil with dedicated 32 Ch Rx array. Rx array with in-laid grid to localize loop geometry. Copper of 32 Rx- array was extracted from CAD models to verify its effect on Tx coil fields.

Appendix B Solidworks and Other Protypes Built

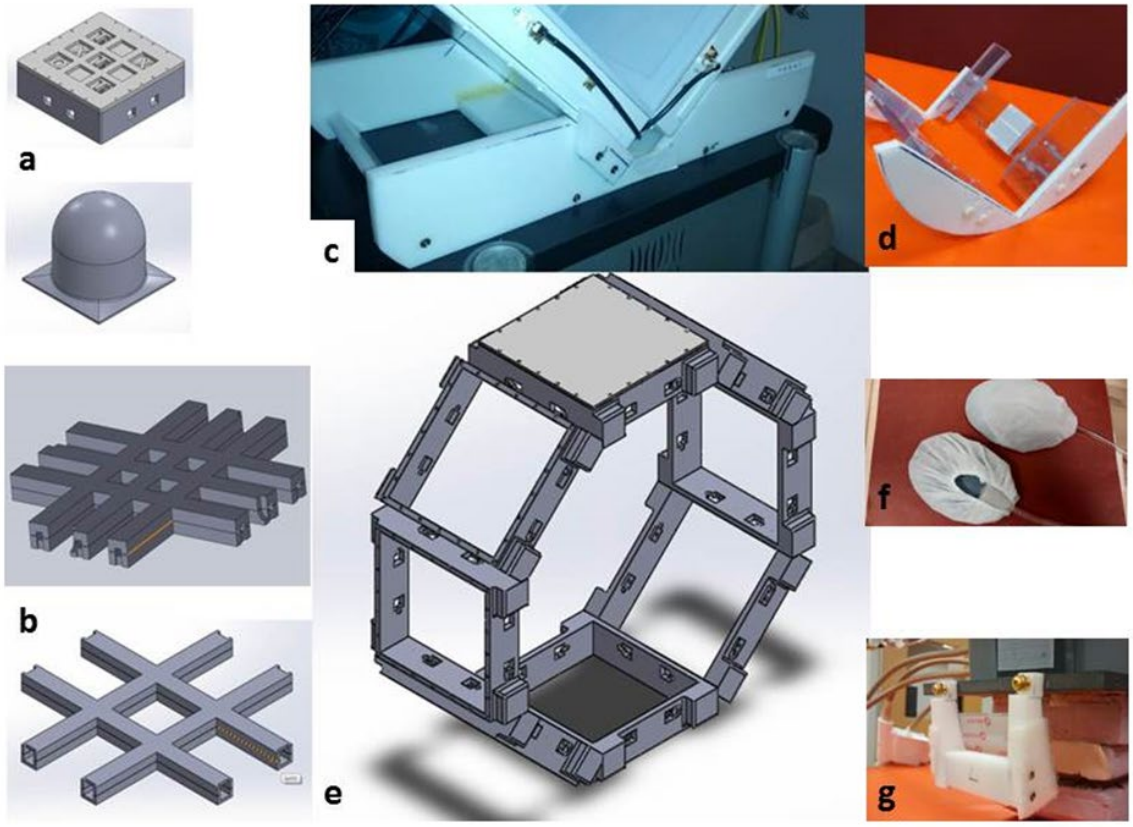

Figure 29: Miscellaneous Prototypes Built: Coil Stands, Boxes, Frames, Struts etc.

Bibliography

1. Lauterbur P. C.; Nobel Lecture. All science is interdisciplinary--from magnetic moments to molecules to men. Biosci Rep. 2004;24(3):165-78. Epub 2005/10/08. PubMed PMID: 16209126.

2. Mansfield P., Pykett I. L.; Biological and medical imaging by NMR. 1978. J Magn Reson. 2011;213(2):513-31. Epub 2011/12/14. doi: 10.1016/j.jmr.2011.09.020. PubMed PMID: 22152367.

3. Tanenbaum L.N.; Clinical 3T MR imaging: mastering the challenges. Magn Reson Imaging. 2006;14(1):1-15. Epub 2006/03/15. doi: 10.1016/j.mric.2005.12.004. PubMed PMID: 16530631.

4. UMN C. Center for Magnetic Resonance Research Seimens 10.5 Magnetom 2013. doi: https://www.cmrr.umn.edu/magnets/105t88.shtml.

5. Wu X., Vaughan J.T., Ugurbil K., Van de Moortele P.F.; Parallel excitation in the human brain at 9.4 T counteracting k-space errors with RF pulse design. Magn Reson Med. 2010;63(2):524-9. Epub 2009/12/18. doi: 10.1002/mrm.22247. PubMed PMID: 20017161; PMCID: PMC3066148.

6. Theysohn J., Maderwald S., Kraff O., Moenninghoff C., Ladd M., Ladd S.; Subjective acceptance of 7 Tesla MRI for human imaging. Magnetic Resonance Materials in Physics, Biology and Medicine. 2008;21(1-2):63-72. doi: 10.1007/s10334-007-0095-x.

7. Kraff O., Fischer A., Nagel A.M., Monninghoff C., Ladd M.E.; MRI at 7 tesla and above: Demonstrated and potential capabilities. J Magn Reson Imaging. 2014:. Epub 2014/01/31. doi: 10.1002/jmri.24573. PubMed PMID: 24478137.

8. Krishnamurthy N., Zhao T., Ibrahim T.S.; Effects of receive-only inserts on specific absorption rate, B1 (+) field, and Tx coil performance. Journal of magnetic resonance imaging. 2014;39(2):475-84. Epub 2013/08/06. doi: 10.1002/jmri.24152. PubMed PMID: 23913474; PMCID: 4501854.

9. Krishnamurthy N., Santini T., Wood S., Kim J., Zhao T., Aizenstein H.J., Ibrahim T.S.; Computational and experimental evaluation of the Tic-Tac-Toe RF coil for 7 Tesla MRI. PLOS ONE. 2018;10.1371/journal.pone.0209663.

10. Westbrook C., Roth C.K., Talbot J.; MRI in Practice. Wiley 2005;3rd Edition.

11. Vaughan J.T., Griffiths J.R.; RF coils for MRI. 1 ed: John Wiley & Sons; 2012.

12. Adriany G., Van de Moortele P-F, Wiesinger F., Moeller S., Strupp J.P., Andersen P., Snyder C., Zhang X., Chen W., Pruessmann K.P., Boesiger P., Vaughan T., Uğurbil K.; Transmit and receive transmission line arrays for 7 Tesla parallel imaging. Magnetic Resonance in Medicine. 2005;53(2):434-45. doi: 10.1002/mrm.20321.

13. Keil B., Triantafyllou C., Hamm M., Wald L.L.; Design Optimization of a 32-Channel Head Coil at 7T ISMRM. 2010:6960. Epub 2010/07/23.

14. Robitaille P-ML, Abduljalil A.M., Kangarlu A., Zhang X., Yu Y., Burgess R., Bair S., Noa P., Yang L, Zhu H, Palmer B, Jiang Z, Chakeres DM, Spigos D.; Human magnetic resonance imaging at 8 T. NMR Biomed. 1998;11(6):263-5.

15. Lattanzi R, Sodickson D.K., Grant A.K., Zhu Y.D.; Electrodynamic Constraints on Homogeneity and Radiofrequency Power Deposition in Multiple Coil Excitations. Magnetic Resonance in Medicine. 2009;61(2):315-34. doi: Doi 10.1002/Mrm.21782. PubMed PMID: ISI:000262871300010.

16. Ercan A.E., Techawiboonwong A., Versluis M.J., Webb A.G., Ronen I.; Diffusion-weighted chemical shift imaging of human brain metabolites at 7T. Magn Reson Med. 2014:doi:10.1002/mrm.25346 Epub 2014/07/06. doi: 10.1002/mrm.25346. PubMed PMID: 24986121.

17. Li. M, Jin J., Zuo Z., Liu. F., Trakic A., Weber E., Zhuo Y., Xue R., Crozier S.; In vivo Sensitivity Estimation and Imaging Acceleration with a Rotating RF Coil Arrays at 7 Tesla. Journal of Magnetic Resonance. 2014 doi: http://dx.doi.org/10.1016/j.jmr.2014.12.004.

18. Sohn S-M, DelaBarre L., Gopinath A., Vaughan J.T.; RF Head coil design with improved RF magnetic near-fields uniformity for magnetic resonance imaging (MRI) systems. IEEE transactions on microwave theory and techniques. 2014;62(8):1784-9.

19.

Yee.K.S.;Numerical solution of the initial boundary value problems involving Maxwell's equations in isotropic media. IEEE Trans Microwave Theory and Techniques. 1966;44:61-9.

20. Gabriel S., Lau R.W., Gabriel C.; The dielectric properties of biological tissues: II. Measurements in the frequency range 10 Hz to 20 GHz. Phys Med Biol. 1996;41(11):2251-69. Epub 1996/11/01. PubMed PMID: 8938025.

21. Gabriel C., Gabriel S., Corthout E.; The dielectric properties of biological tissues: I. Literature survey. Physics in Medicine & Biology. 1996;41(11):2231.

22. Gabriel S., Lau R.W., Gabriel C.; The dielectric properties of biological tissues: II. Measurements in the frequency range 10 Hz to 20 GHz. Physics in Medicine & Biology. 1996;41(11):2251.

23. Gabriel S., Lau R.W., Gabriel C.; The dielectric properties of biological tissues: III. Parametric models for the dielectric spectrum of tissues. Physics in Medicine & Biology. 1996;41(11):2271.

24. Fiedler T.M, Ladd M.E, Bitz A.K.; SAR Simulations & Safety. Neuroimage. 2018;168:33-58. Epub 2017/03/25. doi: 10.1016/j.neuroimage.2017.03.035. PubMed PMID: 28336426.

25. Liu F., Zhao H., Crozier S.; On the Induced Electric Field Gradients in the Human Body for Magnetic Stimulation by Gradient Coils in MRI. IEEE Trans Biomedical engineering. 2003;50(7).

26. Liu F., Zhao H., Crozier S.; Calculation of electric fields induced by body and head motion in high-field. J Magn Reson Imaging. 2003;161:99-107.

27. Wiggins G., Wiggins C., Potthast A., Alagappan V., Kraff O., Reykowski A., Wald L. A. 32 channel receive-only head coil and detunable transmit birdcage coil for 7 Tesla brain imaging. ISMRM. 2006;Seattle USA.

28. Wiggins G.C., Polimeni J.R., Potthast A., Schmitt M., Alagappan V., Wald L.L.; 96-Channel receive-only head coil for 3 Tesla: design optimization and evaluation. Magn Reson Med. 2009;62(3):754-62. Epub 2009/07/23. doi: 10.1002/mrm.22028. PubMed PMID: 19623621; PMCID: 2915832.

29. Angelone L.M., Potthast A., Segonne F., Iwaki S., Belliveau J.W., Bonmassar G.; Metallic electrodes and leads in simultaneous EEG-MRI: specific absorption rate (SAR) simulation studies. Bioelectromagnetics. 2004;25(4):285-95. Epub 2004/04/29. doi: 10.1002/bem.10198. PubMed PMID: 15114638.

30. Angelone L.M., Vasios C.E., Wiggins G., Purdon P.L., Bonmassar G.; On the effect of resistive EEG electrodes and leads during 7 T MRI: simulation and temperature measurement studies. Magn Reson Imaging. 2006;24(6):801-12. Epub 2006/07/11. doi: 10.1016/j.mri.2006.01.006. PubMed PMID: 16824975.

31. Oh S., Ryu Y., Wang Z., Robb F., Collins C.M.; Influence of a Receive-array Coil on Specific Absorption Rate at 3T: Simulations and Experiments with Basic Geometries ISMRM. 2010.

32. Taflove A., Hagness S.C.; Computational Electrodynamics: The Finite-Difference Time-Domain Method. Artech House. 2005;Third Edition.

33. Ibrahim T.S., Hue Y.K., Tang L.; Understanding and manipulating the RF fields at high field MRI. NMR Biomed. 2009;22(9):927-36.

34. Jean-Pierre B. Three-Dimensional Perfectly Matched Layer for the Absorption of Electromagnetic Waves. Journal of Computational Physics. 1996;127(2):363-79. doi: 10.1006/jcph.1996.0181.

35. Hand J.W.; Modelling the interaction of electromagnetic fields (10 MHz–10 GHz) with the human body: methods and applications. Physics in Medicine and Biology. 2008;53(16):R243.

36. Ibrahim T.S., Abduljalil A.M., Baertlein B.A., Lee R., Robitaill P.M.; Analysis of B1 field profiles and SAR values for multi-strut transverse electromagnetic RF coils in high field MRI applications. Phys Med Biol. 2001;46(10):2545-55. Epub 2001/11/01. PubMed PMID: 11686274.

37. Bottomley P.A., Redington R.W., Edelstein W.A., Schenck J.F.; Estimating radiofrequency power deposition in body NMR imaging. Magn Reson Med. 1985;2(4):336-49. Epub 1985/08/01. PubMed PMID: 4094551.

38. Shellock F.G.; Radiofrequency energy-induced heating during MR procedures: a review. J Magn Reson Imaging. 2000;12(1):30-6. Epub 2000/08/10. PubMed PMID: 10931562.
39. Chen X., Hamamura Y., Steckner M.; Numerical simulation of SAR for 3T whole body coil: effect of patient loading positions on local SAR hotspot. ISMRM. 2010;Stockholm Sweden.

40. Hue Y-K, Ibrahim T.S., Zhao T., Boada F.E., Qian Y.; A Complete Modeling System with Experimental Validation for Calculating the Transmit and Receive Fields, Total Power Deposition, Input Impedance, and Coupling between Coil Elements. ISMRM. 2008:0438.

41. Oakton Con 110; Conductivity Meter. http://www4oaktoncom/proddetailasp?parent=52&prod=320&TotRec=19&Seq=4&qty=0.

42. SPEAG. Dielectric Assessment Kit. Zurich, Switzerland. doi: http://www.speag.com/products/dak/dielectric-measurements/.

43. Krishnamurthy N., Zhao T., Stough D., Raval S., Boada F., Ibrahim T.S.; B1+ and Coupling Variability of Transmit Head Coils and Arrays for Ultra-High Field MRI: Simulation Studies and Experiments. ISMRM Melbourne. 2012.

44. Wang C., Shen G.X.; B1 field, SAR, and SNR comparisons for birdcage, TEM, and microstrip coils at 7T. J Magn Reson Imaging. 2006;24(2):439-43. Epub 2006/06/21. doi: 10.1002/jmri.20635. PubMed PMID: 16786582.

45. Vaughan J.T, Hetherington H.P, Otu J.O., Pan J.W., Pohost G.M.; High frequency volume coils for clinical NMR imaging and spectroscopy. Magnetic Resonance in Medicine. 1994;32(2):206-18. doi: 10.1002/mrm.1910320209.

46. Ibrahim T.S., Raval S., Krishnamurthy N., Wood, S., Kim, J-H., Zhao, Y., Wu, X. S., Yacoub, E.S, Aizenstein, H.S. and Zhao. T.; Towards Homogeneous 7T Neuro Imaging: Findings and Comparisons between 7T TTT and NOVA RF Coil Systems. ISMRM. 2017;http://cds.ismrm.org/protected/17MPresentations/abstracts/4403.html(4403).

47. Santini T., Zhao Y., Wood S., Krishnamurthy N., Kim J., Farhat N., Alkhateeb S., Martins T., Koo M., Zhao T., Aizenstein H.J., Ibrahim T.S.; In-vivo and numerical analysis of the eigenmodes produced by a multi-level Tic-Tac-Toe head transmit array for 7 Tesla MRI. PLOS ONE. 2018;13(11):e0206127. doi: 10.1371/journal.pone.0206127.

48. Zhao,Y., Zhao, T., Raval, S.B., Krishnamurthy, N. , Zheng , H., Chad T. Harris , William B. Handler , Blaine A. Chronik , and Ibrahim, T.S.; Dual Optimization Method of RF and Quasi-Static Field Simulations for Reduction of Eddy Currents Generated on 7T RF Coil Shielding. MRM. 2014:DOI: 10.1002/mrm.25424.

49. Santini T., Kim J., Wood S., Krishnamurthy N., Farhat N., Maciel C., Raval, S.B., Zhao, Ibrahim T.S.; A new RF transmit coil for foot and ankle imaging at 7T MRI. MRI. 2018;45(1873-5894 (Electronic)):10.1016/j.mri.2017.09.005. Epub Sept 2017.

50. Kim J., Krishnamurthy N., Santini T., Zhao Y., Zhao T., Bae K.T., Ibrahim T.S. ; Experimental and numerical analysis of B1+ field and SAR with a new transmit array design for 7T breast MRI. J Magn Reson. 2016;269:55-64. Epub 2016/05/31. doi: 10.1016/j.jmr.2016.04.012. PubMed PMID: 27240143.

51. Kim J., Santini T., Bae K.T., Krishnamurthy N., Zhao Y., Zhao T., Ibrahim T.S.; Development of a 7 T RF coil system for breast imaging. NMR in Biomedicine. 2017;30(1):e3664-n/a. doi: 10.1002/nbm.3664.

52. Bitz A., Brote I., Orzada S., Kraff O., Maderwald S., Quick H., Solbach K., Bahr A., Fautz H., Schmitt F.,; Comparison of simulation-based and measurement-based RF shimming for whole-body MRI at 7 Tesla. Proceedings of the 18th Annual Meeting of ISMRM, Stockholm, Sweden; 2010.

53. Homann H, Graesslin I., Eggers H., Nehrke K., Vernickel P., Katscher U., Dössel O., Börnert P.; Local SAR management by RF shimming: a simulation study with multiple human body models. Magnetic Resonance Materials in Physics, Biology and Medicine. 2012;25(3):193-204.

54. Christ A., Kainz W., Hahn E.G., Honegger K., Zefferer M., Neufeld E., Rascher W., Janka R., Bautz W., Chen J., Kiefer B., Schmitt P., Hollenbach H.P, Shen J.X, Oberle M, Szczerba D, Kam A, Guag JW, Kuster N. The Virtual Family-development of surface-based anatomical models of two adults and two children for dosimetric simulations. Physics in Medicine and Biology. 2010;55(2):N23-N38. doi: Doi 10.1088/0031-9155/55/2/N01. PubMed PMID: WOS:000272960400015.

55. Ibrahim T.S., Stough D., Zhao T.; 20-Ch Tx Modular Array for 7T PTX Applications. ISMRM. 2012;2807.

56. Ibrahim T.S., Hue Y.K., Tang L.; Understanding and manipulating the RF fields at high field MRI. Nmr in Biomedicine. 2009;22(9):927-36. doi: Doi 10.1002/Nbm.1406. PubMed PMID: WOS:000271806300004.

57. Tang L, Hue Y. K, Ibrahim T.S.; Studies of RF Shimming Techniques with Minimization of RF Power Deposition and Their Associated Temperature Changes. Concepts Magn Reson Part B Magn Reson Eng. 2011;39B(1):11-25. Epub 2011/05/25. doi: 10.1002/cmr.b.20185. PubMed PMID: 21607117; PMCID: 3098508.

58. FSL. Brain Extraction Tool of FMRIB Software Library, http://fsl.fmrib.ox.ac.uk/fsl/fslwiki/BET.

59. Insight Toolkit I. ITK-SNAP http://www.itksnap.org/pmwiki/pmwiki.php.

60. Tilley A.R. The measure of man and woman, human factors in design. John Wiley & Sons. 2002:p27.